Characterizing filaments harboring high-mass star formation

Carlos Roberto Gutiérrez Chaves

Advisors:

Gemma Busquet

Robert Estalella

UNIVERSITAT DE BARCELONA

Master in Astrophysics Particle Physics and Cosmology

Universitat de Barcelona

Faculty of Physics

Deparment of Quantum Physics and Astrophysics

September 2017

Contents

1 Introduction

1.1 General View of Infrared Dark Clouds

A distinguished kind of molecular clouds, the infrared dark clouds (hereafter IRDCs), are believed to be relevant for describing the initial conditions for high-mass star formation. They are characterized by their lack of detectable emission in the mid-infrared: they appear as a dark silhouette against the corresponding mid-infrared background. IRDCs were first recognized in images from the *Infrared Space Observatory* (ISO, Egan et al. 1998) and the *Midcourse Space Experiment* (MSX, Perault et al. 1996).

Properties of IRDCs are widely described in early works by Carey et al. (1998) and later by Pillai et al. (2006) and Rathborne, Jackson and Simon (2006) listing typical gas temperatures of < 20 K, densities larger than 10^6 cm^{-3}, column densities larger than 10^{22} cm^{-2} and masses in the 10^2– 10^3 M$_\odot$ range. The variety of morphologies for IRDCs ranges from the most commonly observed filamentary structures to an apparent spherical distribution (e.g. Ragan, Bergin and Gutermuth 2009; Butler and Tan 2009).

Based on the corrrelation between the ^{13}CO line emission and mid-infrared (MIR) extinction through the MSX survey towards hundreds of IRDCs, Simon, Jackson, Rathborne et al. (2006a, 2006b) find that most of the IRDCs concentrate in what is known as the Galactic ring at a galactocentric radius of 5 kpc, and their kinematic distances typically range from 2 - 9 kpc.

1.2 Filamentary Structures

Filaments are ubiquitous structures in both low- and high-mass star-forming regions (e.g. Hatchell et al. 2005, Jackson et al. 2010). They can be identified in the mid-IR as IRDCs, as well as in emission at far-IR wavelengths (e.g. André et al. 2010; Molinari et al. 2010). Filaments were recognized more than 30 years ago (Schneider and Elmegreen 1979) but the omnipresence of such structures in star-forming complexes, as revealed by *Herschel* surveys, triggered again special attention on their formation mechanism and their role in the star formation process.

Prior to the *Herschel* launch, only a few observational studies have focused on the physical properties of filaments and their relation to star-formations processes (e.g. Goldsmith et al. 2008, Myers 2009). Next, with the arrival of *Herschel* some new light was shed about the complex morphologies of filaments through the systematic and statistical analysis in multiple molecular clouds along with measurements of intrinsic parameters such as the mass, column densities and dust temperatures (e.g. Molinari et al. 2010; Arzoumanian et al. 2011). Despite of this, the information provided by *Herschel* did not described fundamental kinematical properties of these structures such as their velocity field and dynamical stability.

There are multiple scenarios for the formation of filaments: *i)* they may form due to the dissipation of supersonic turbulent motions from dense gas (e.g. Padoan et al. 2001; Arzoumanian et al. 2011); *ii)* through collisions at large scale between filaments or through substructures formed in the turbulent cloud that end up converging one onto another (e.g. Jiménez-Serra et al. 2010; Nakamura et al. 2012; Henshaw et al. 2013); *iii)* formation through global gravitational contraction of molecular clouds and their filaments and cores (e.g. Schneider et al. 2010, Gómez and Vázquez-Semadeni 2014).

Filamentary structures are widely analysed in a review work centered in the results of the *Gould Belt Survey,* a Herschel key project to perform photometric studies in the nearby star-forming regions, written by André et al. (2014). Accordingly with this review, these filaments have lengths ranging from ~ 1 to tens of pc, and although there have been found some small scale deviations, the overall filamentary structures are very linear over their lengths, meaning that they follow a unique direction with minimal curvatures and no sharp changes. What is even more interesting is that, some clouds that appear to be filamentary globally also exhibit populations of sub-filaments inside their structure, these subfilaments are called fibers (Hacar et al. 2013).

Although the *Herschel* era has given valuable photometric information, molecular line studies are extremely important since they provide precious information for unveiling the real structure of these filaments and for understanding their main properties such as their kinematics. With this in mind, in this work we analyze the kinematics of two filamentary IRDCs G034.43+00.24 and G035.39-00.33 through observations of the NH_3 molecule in order to obtain their main physical properties and provide a detailed description of their kinematics.

1.3 The IRDC G034.43+00.24

The IRDC G034.43+00.24 (hereafter G34) is a portion of the Giant Molecular Filament GMF38.1–32.4a, it has a remarkable filamentary morphology and the distance to this IRDC was determined to be 1.56 ± 0.12 kpc by VLBI maser-parallax observations (Kurayama et al. 2011).

The kinematic distance used before the Kuruyama et al. determination was 3.7 kpc, and this is the distance still used for the classification and masses of young stellar objects given in Table 1.1. The new value of the distance of 1.56 kpc is used in the analysis presented in this work.

Rathborne et al. (2005) identified, through 1.2 mm dust continuum emission measurements, three potential star-forming clumps to be hosting compact milimeter sources, presumably harboring high-mass protostars.

In subsequent works (Butler and Tan 2009; Rathborne, Jackson and Simon 2006), a total of nine millimeter clumps have been identified. In particular, Rathborne et al. 2005 find that the MM3 clump exhibits signs of star-forming activity and that it harbors a massive protostar of spectral type B0.5; a protostar of the same spectral type is also found in the MM4 clump (see Figure 1.1a). They also find that MM1 clump harbors a central protostellar object thought to be of spectral type O9.5 and that MM2 is associated with the source IRAS 18507+0121 (Xu et al. 2016). For further detailed information on the above mentioned millimeter clumps see Table 1.1.

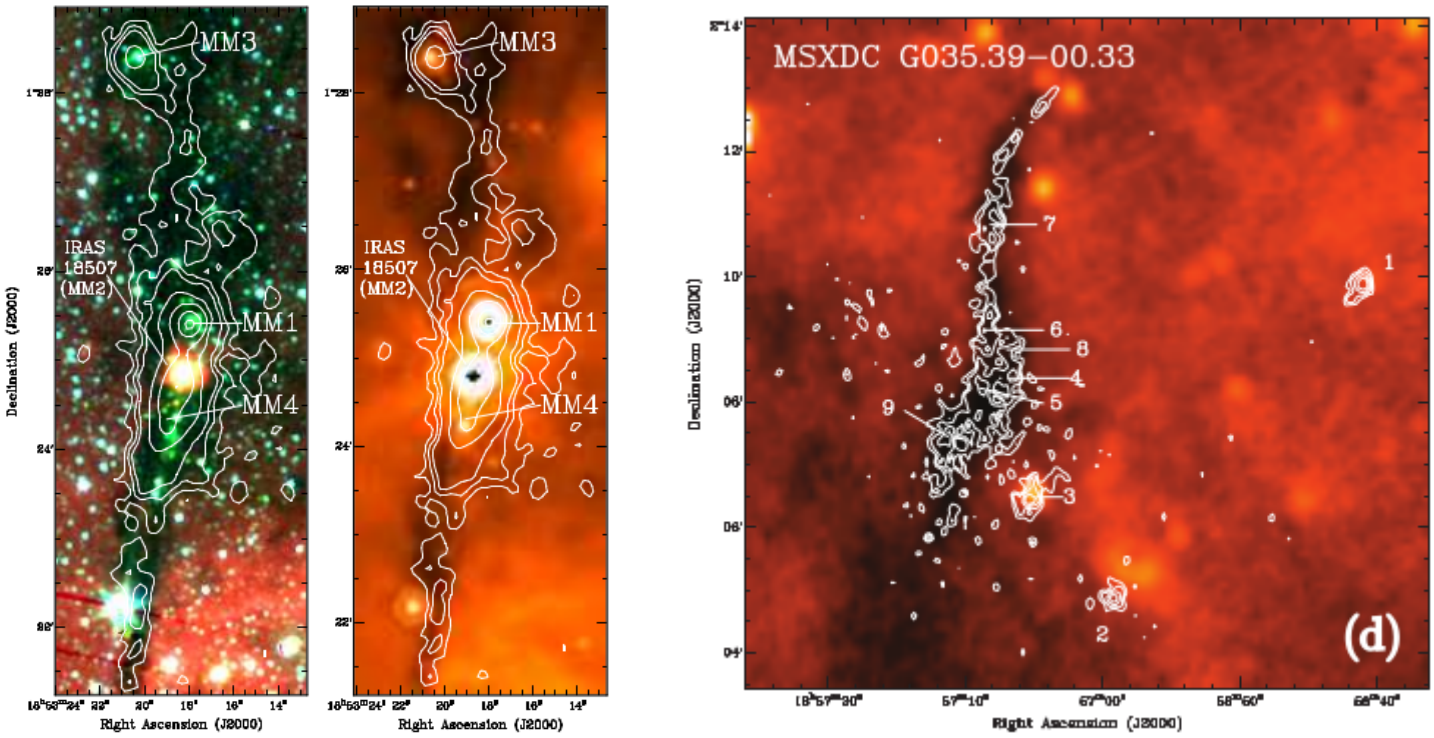

(a) (b)

Figure 1.1: Region G034.43+00.24 (a) Left: *Spitzer*/IRAC three-color image (3.6 μm in blue, 4.5 μm in green and 8.0 μm in red) overlaid with IRAM/MAMBO-II 1.2 mm continuum emission . Right: *Spitzer*/MIPS 24 μm image with contours of the IRAM/MAMBO-II 1.2 mm continuum emission. Image from Rathborne et al. (2005). Region G035.39-00.33 (b) MSX 8 μm image overlaid with 1.2 mm continuum emission; the contours in all cases are 30 ($\sim 3\sigma$), 60, 90, 120, 240, 360, 480, 840, 1200, and 2400 mJy beam^{-1} . Images from Rathborne, Jackson and Simon (2006).

1.4 The IRDC G035.39-00.33

The IRDC G035.39-00.33 (hereafter G35) has extremely filamentary morphology along with extended quiescent regions and is located at a kinematic distance of 2.9 kpc with a central velocity $v_{\rm LSR} = 44.7\,{\rm km\,s^{-1}}$ (Simon, Rathborne, Shah et al. 2006b). Butler and Tan (2009) and Rathborne, Jackson and Simon (2006) identified nine millimeter clumps whose characteristics vary depending on their location within the cloud (see Figure 1.1b).

Henshaw et al. (2013) find that the southern portion of the cloud appears to be associated with star formation activity because of the prescence of 8 and 24 μm sources. The most massive cores are MM6, MM7 and MM8 in Rathborne, Jackson and Simon (2006), which are in the northern portion of the cloud. Further characteristics of these millimeter clumps are listed in Table 1.1.

Based on molecular line emission observations, Henshaw et al. (2013, 2014) find that G35 can be seen as a composition of different filaments with varying densities and large-scale small velocity gradients: Filament 1 ($v_{\rm LSR} \sim 42.95 \pm 0.17\,{\rm km\,s^{-1}}$), which appears as a low-density blueshifted filament, Filament 2 ($v_{\rm LSR} \sim 45.63 \pm 0.03\,{\rm km\,s^{-1}}$), which is the main filamentary structure of the cloud and Filament 3 ($v_{\rm LSR} \sim 46.00 \pm 0.06\,{\rm km\,s^{-1}}$),

which is red-shifted. It is also noted that Filament 2 presents an abrupt change in velocity interpreted as the entanglement between two sub-filamentary structures: F2a ($v_{\rm LSR} \sim 45.34 \pm 0.04$ km s^{-1}) and F2b ($v_{\rm LSR} \sim 46.00 \pm 0.05$ km s^{-1}).

1.5 Aim

The aim of the present work is to give a detailed description of the kinematics of G34 and G35 through analysis of previously calibrated NH_3 data (see section 2.2 for details of the observations and reduction process). This was done using a code called Hyperfine Structure Fitting Tool (Hfs) developed by Estalella (2017); the results listing the physical parameters obtained from the regions are explained throughout Chapter 3 meanwhile the discussion of derived properties of the IRDCs such as stability and comparison with other works are confined in Chapter 4.

TABLE 1.1: MILLIMETER CLUMP CHARACTERISTICS

Region	Clump[a]	R.A (J2000) (h:m:s)	Decl (J2000) (°:′:″)	Type[b]	Mass[c] $(M_\odot)$
	MM1	18 53 18.0	01 25 24	Prestellar	1187
	MM2	18 53 18.6	01 24 40	Protostellar	1284
	MM3	18 53 20.4	01 28 23	Protostellar	301
	MM4	18 53 19.0	01 24 08	Protostellar	253
G034.43+00.24	MM5	18 53 19.8	01 23 30	Prestellar	664
	MM6	18 53 18.6	01 27 48	Prestellar	126
	MM7	18 53 18.3	01 27 13	Prestellar	87
	MM8	18 53 16.4	01 26 30	Prestellar	108
	MM9	18 53 18.4	01 28 14	Prestellar	157
	MM1	18 56 41.2	02 09 52	Protostellar	76
	MM2	18 56 59.2	02 04 53	Protostellar	45
	MM3	18 57 05.3	02 06 29	Protostellar	79
	MM4	18 57 06.7	02 08 23	Prestellar	108
G035.39-00.33	MM5	18 57 08.8	02 08 09	Protostellar	118
	MM6[d]	18 57 08.4	02 09 09	Protostellar	71
	MM7[c]	18 57 08.1	02 10 50	Protostellar[e]	96
	MM8[c]	18 57 07.0	02 08 54	Prestellar	59
	MM9	18 57 11.2	02 07 27	Prestellar	42

[a] Millimetric clumps identified by Rathborne, Jackson and Simon (2006).

[b] Based on types of clumps stated in Rathborne et al. (2005) and Nguyen Luong et al. (2011)

[c] The mass values are calculated by Rathborne, Jackson and Simon (2006) using

$$M = \frac{F_\nu D^2}{\kappa_\nu B_\nu(T)}$$

where F_ν is the flux density, D is the distance and κ_ν is the dust opacity per gram of dust. Calculation was done adopting a dust opacity at 1.2 mm of 1.0 cm^2 g^{-1} and a dust-mass ratio of 100. A graybody emission with emissivity index of $\beta = 2$ and kinematic distances to G34 and G35 of 3.7 and 2.9 kpc were also assumed.

[d] Correspond to Clumps H5, H6 and H4 described in Henshaw et al. (2013, 2014)

[e] Clump associated with source IRAS 18507+0121

2 Observations

2.1 The Ammonia Tracer

Due to the fact that the NH_3 structure is very well known and that its energy transitions are rather complicated in comparison with other molecules, it provides a lot of information which makes it an excellent gas tracer for studying the physical conditions in dense regions in molecular clouds (Ho and Townes 1983; Estalella and Anglada 1996).

The ammonia molecule has hyperfine structure which makes possible to obtain different physical parameters such as opacity from just one observation and without the need of observing other isotopes. Because of quantum tunneling effects due to its pyramidal structure, its energy levels are splitted into inversion doblets which makes energy transitions between sublevels to correspond to energy changes in the centimeter part of the electromagnetic spectrum instead of falling in the infrared.

Furthermore, because of effects of the interaction between the electric field and the nitrogen atom, these doblets are at the same time splitted into three sublevels making it possible for 6 other transitions to occur. Finally, each of these sublevels are splitted into other five hyperfine sublevels because of the quadrupolar electric momentum interactions, making the final total number of components for the inversion transition to be 18, although it is impossible to distinguish all the lines and therefore it is only likely to observe a hint of these hyperfine structure states (Ho and Townes 1983; Sepúlveda 1993; Estalella and Anglada 1996).

The main factors, appart from its hyperfine structure, which make this molecule an ideal tracer for developing a study of dense regions in molecular clouds are:

1. It is very easy to detect as it is a relatively abundant component of the molecular clouds, its abundance is estimated to range as $\left[\frac{NH_3}{H_2}\right] \sim 10^{-9}$– 10^{-7} (e.g. Ungerechts, Winnewisser and Gaida 1985; Pillai et al. 2006; Foster et al. 2009).
2. The critical density of thermalization of these transitions is of the same order of magnitude that the density of dense cores in molecular clouds ($n_{\rm crit} \simeq 5 \times 10^3\,{\rm cm}^{-3}$, Estalella and Anglada 1996).
3. The inversion lines of the rotational states have very near frequencies making possible to observe their emission with the same instrument and almost identical angular resolution; for example the frequencies for the $NH_3(1,1)$ and $NH_3(2,2)$ transitions are 23.69 GHz and 23.72 GHz respectively (Ho and Townes 1983; Sepúlveda 1993).
4. The NH_3 molecule gets excited at low temperatures which coincide with the usual temperatures present in molecular clouds ($T \leq 20\,{\rm K}$).

TABLE 2.1: GBT FILAMENT OBSERVATION DETAILS

Region	R.A (J2000) (h:m:s)	Decl (J2000) (°:′:″)	d (kpc)	$v_{\rm LSR}$ $\left(\mathrm{km\,s^{-1}}\right)$	map size (arcmin×arcmin)	rms noise (K)	Project Code
G034.43+00.24	18 53 18.9	01 26 38	1.56	57.1	4.2×9.4	0.09	GBT12B-283
G035.39-00.33	18 57 10.4	02 08 27	2.90	45.5	4.2×8.8	0.08	GBT13A-054

2.2 Green Bank Observations

The observations of the $NH_3(J, K) = (1, 1)$ and (2,2) inversion line transitions toward the 2 filaments were carried out using the 100 m Robert C. Byrd Green Bank Telescope (GBT) of the NRAO[a], located near Green Bank (WV, USA), during different observing runs between 2013 March and May for G035.39-00.33 (project code: GBT13A-054; P.I. Gemma Busquet). We additionally used the archival data for filament G34.43+00.24 (project code: GBT12B-283). Such information along with details of the observations are listed in Table 2.1.

The K-band Focal Plane Array (KFPA) receiver was used as a front end with 2 feeds and dual circular polarization. The GBT spectrometer was used as a backend to simultaneously observe all lines in separate IFs bandwidth of 50 MHz, each one with 4096 channels, giving a frequency resolution of 12.207 kHz or 0.154 $\mathrm{km\,s^{-1}}$ at 23.6945 GHz.

The data were collected using the on-the-fly (OTF) mapping mode and using the in-band frequency switching with a throw of 7.5 MHz. All maps were made alternating the scanning direction (R.A. and DEC.) to avoid artificial striping in the data cubes. The telescope Full Width at Half Maximum (FWHM) beam was approximately 32″. For each map, rows/columns were spaced by 13″ in R.A or DEC. to ensure Nyquist sampling, while for a fixed row/column the dump rate was 4 dumps per beam, and producing a dump every 2 seconds. Pointing was checked at hourly intervals on a nearby quasar, with corrections approximately $2'' - 3''$. Flux calibration was performed on NGC 7027, with a flux accuracy of $\sim$ 10–20 %. System temperatures ($T_{\rm sys}$) ranged from 38 to 60 K during the observing dates. The average system temperature for the project GBT12B-283 was 46.3 K.

The zenith opacity was obtained for each observing run using a local weather model. The GBT main beam efficiency ($\eta_{\rm MB}$) is 0.81 at the NH_3 $(1, 1)$ and $(2, 2)$ line frequencies. These values were used to convert the data to units of main beam temperature, $T_{\rm MB}$. Final maps were obtained using the GBT Mapping Pipeline[b]. Briefly, it calibrates the spectral line data using the GBTIDL package[c]. Then, the idlToSdfits command converts SDFITS format that can be read by AIPS. Data were then combined with the DBCON, and the resulting data cubes were then converted into FITS files.

[a]The National Radio Astronomy Observatory is a facility of the National Science Foundation operated under cooperative agreement by Associated Universities, Inc.

[b]https://safe.nrao.edu/wiki/bin/view/GB/Gbtpipeline/PipelineRelease

[c]GBTIDL is an interactive package for reduction and analysis of spectral line data taken with the GBT. See: http://gbtidl.nrao.edu

3 Methodology and Results

3.1 Methodology

In the present work we used the Hyperfine Structure Fitting Tool (Hfs) program developed by Estalella (2017) to perform a pixel by pixel simultaneous fitting of $NH_3(1,1)$ and $NH_3(2,2)$ hyperfine inversion transitions for G34 and G35.

In order to fit the lines, the program requires some input parameters: the signal to noise ratio (SNR), the rms of the data, the number of velocity components considered for each region and the velocity range for each velocity component. For G34 and G35 we used three and four velocity component ranges respectively. We fitted only those positions with a SNR greater than 4 for $NH_3(1,1)$ and 3 for $NH_3(2,2)$. Further information on the details for the fitted velocity components are summarized in Table 3.1.

For each IRDC two runs of the program were performed; the first one to fit simultaneously the hfs for both the $NH_3(1,1)$ and $NH_3(2,2)$ lines to obtain the physical parameters such as column density $N(NH_3)$ and rotational temperature $T_{\rm rot}$. The second run was performed to obtain a complete description of the kinematics through a sole fitting of the $NH_3(1,1)$ transition; as a result parameters such as the central velocity v_{LSR} and linewidth Δv for each velocity components could be obtained in a larger area.

3.1.1 Parameters

The Hfs procedure provides FITS images and ASCII files with the fitted and derived line parameters as well as the NH_3 physical parameters for each velocity component. A full desription of the fitted and derived line parameters is provided in Estalella (2017), here we make a simplified summary.

Fitted Line Parameters

The fitted parameters from the $NH_3(1,1)$ hyperfine line transition are:

1. The hyperfine line linewidth, assumed to be the same for all the hyperfine lines, denoted ΔV.
2. The main line central LSR velocity V_{LSR}.
3. The main line peak intensity A^*_m, which is related with the amplitude A of the line, for hyperfine lines wider than the hyperfine separation and the channels width, by $A^*_m = A\,(1 - \exp(-\tau_m))$.
4. The quantity $\tau^*_m = 1 - \exp(-\tau_m)$, with τ_m being the optical depth of the line.

TABLE 3.1: VELOCITY COMPONENTS

Region	Number of components	Velocity Range $\left(\mathrm{km\,s^{-1}}\right)$
G034.43+00.24	1	53.9 – 57.1
	2	57.4 – 58.7
	3	59.0 – 60.7
G035.39-00.3	1	41.8 – 43.1
	2	43.5 – 44.4
	3	44.7 – 46.7
	4	47.0 – 47.6

When the $NH_3(2,2)$ hyperfine line transition is taken into account, two additional parameters are fitted:

5. The $NH_3(2,2)$ transition central LSR velocity, V_{LSR2}.
6. The $NH_3(2,2)$ transition main line peak intensity A^*_{2m}, calculated in the same way that A^*_m, but taking into account τ_{2m}

Derived Line Parameters

From the fitted parameters presented above, Hfs derives the main line parameters as the amplitude A, the main line optical depth τ_m and the amplitude multiplied by the main line optical depth $A\tau_m$.

Physical Parameters from the NH_3

The procedures also proportionates another set of parameters of more physical nature, assuming that the region is homogeneous along the line of sight. These derived physical parameters are: the rotational temperature T_{rot}, the beam-averaged ammonia column density $fN(NH_3)$ where f is the beam filling factor assumed to be 1, the $NH_3(1,1)$ and $NH_3(2,2)$ beam-average column densities $fN(1,1)$ and $fN(2,2)$, and the kinetic temperature T_{k}.

3.1.2 Fitted Spectra

Although the Hfs program through its different procedures makes available an important quantity of parameters it is unreasonable to think that the spectra fitted through all the pixels will be perfect. There are actually some circumstances in which the fitted velocity components could give a wrong set of parameters due to their poor adjustment. Some of these reasons are:

- The procedure might fit pixels in which the signal is noisy, which happens mostly in the regions close to the edges of the map due to lower sampling in the RA/DEC OTF maps.

- Components with too large and too small linewidths are usually bad fitted. This occurs because although there are well defined velocity ranges for each of the components, excess in emission and near velocity peaks can alter the fit, making it to be very large, or if there is signal of emission similar to the rms, the resulting fitting provides a very small linewidth.
- Regions of high opacity will saturate the velocity component fit and the obtained values from it would be unreliable.

3.1.3 Blanking

Due to the problems listed above a post-processing procedure was applied to blank the pixels that produced a bad or not reliable fit. This was done for each IRDC separately.

For both clouds the criteria to find the different cutoff blanking values was the following: for linewidths (Δv) the fitted spectra was analysed component by component in order to find the values between which the adjustment of the components was acceptable; for the intensity corrected by opacity ($A\tau_m$) the principle employed was that velocity-component spectra fitted for a value of this parameter less than the product of the signal to noise ratio and the rms would be negiglible. Lastly, for the error in central velocity (v_{LSR}) it was taken into account that an error higher than 3.0 $\mathrm{km\,s^{-1}}$ would mean a wrong determination of the velocity component fit.

Blanking in G34 fitted spectra was performed for values in linewidth outside the range $0.4 < \Delta v < 3.0$ $\mathrm{km\,s^{-1}}$, for $A\tau_m$ values less than 0.36 and errors in v_{LSR} larger than 3.0 $\mathrm{km\,s^{-1}}$.

In the case of G35 the same parameters were taking into account for performing the blanking but with a different set of cutoff values; values out of a linewidth range of $0.2 < \Delta v < 2.0$ $\mathrm{km\,s^{-1}}$ were blanked along with values with $A\tau_m$ less than 0.32, also blanking was done for values of error in v_{LSR} larger than 3.0 $\mathrm{km\,s^{-1}}$.

3.2 Results

Figure 3.1 shows the zero-order moment map of $NH_3(1,1)$ and $NH_3(2,2)$ overlaid on the 8 μm *Spitzer* image for G34 (left panel) and G35 (right panel); the integration has been done taken into account the main and the sattelite lines. The overall morphology of G34 consists of an extended and filamentary structure elongated in the north-south direction, harboring three NH_3 peaks which appear to coincide with the MM1, MM2 and MM3 millimeter clumps identifed in Rathborne, Jackson and Simon (2006). On the other hand the morphology of G35 is that of a S-shaped filament, elongated following a northwest-southeast direction with three NH_3 emission peaks. There is a clear offset of about $\sim$3" between the NH_3 and the 1.2 mm peaks, which can be related pointing errors.

3.2.1 General review of fitted data

The fitted spectra for G34 consisted in three velocity components (see Figure 3.2), the first one is present mainly in the southern part of the region, the second component can

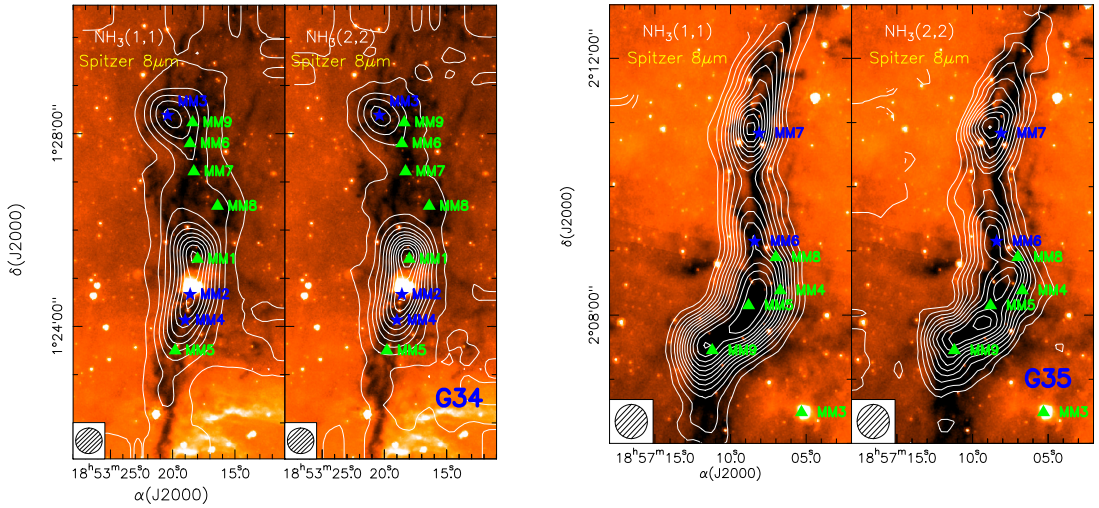

(a) **(b)**

Figure 3.1: G34 and G35 zeroth order moment maps for both the $NH_3(1,1)$ and $NH_3(2,2)$ transitions overlaid with the respective 8 μm *Spitzer* images. For G34 (left panels) contour levels range from 9 to 160 in steps of 12 times the rms noise of the map, 0.32 K km s^{-1}. For G35 (right panels) contour levels range from 9 to 120 in steps of 3 times the rms of 0.36 K km s^{-1}. The location of the 1.2 mm prestellar and protosterllar clumps identified in Rathborne, Jackson and Simon (2006) is represented by green triangles and blue stars respectively.

be seen in the central part of G34 meanwhile the third component is predominantly in the northern region.

Four velocity component fitting for G35 showed interesting features (see Figure 3.3), the main component for this IRDC identified as component 3, extents from northwest to southeast, representing most of the filament. The other three components are scattered at different sites: component 1 is mainly present at the center of the cloud, component 2 is present at the center and through the south whilst component 4 is located at the northern side of the cloud.

3.2.2 Central Velocity and Linewidth Maps

Central velocity maps of G34 can be seen in Figure 3.4 for each one of the three velocity components. It is possible to spot local velocity gradients, for example in the southwest part for component 1 the velocity gradient of 1.153 km s^{-1} pc^{-1} has an overall southwest to northeast direction; the map of this component also reveals gas at the west edge that has relatively high values in velocity (up to 57.32 km s^{-1}). In the northern part of component 2 a velocity gradient of 1.854 km s^{-1} pc^{-1} can be spotted in the southwest to northeast direction. Velocity gradients for component 3 remain unclear due to little presence of this component in the southern part of the cloud. The first and second velocity components clearly present a filamentary structure, and although the third component is elongated in the north-south direction, the poor pixel sampling of the third component prevented us to include this component in the following analysis of filamentary structures. Thus, in the following we include only component 1 and 2 for the filament analysis of G34.

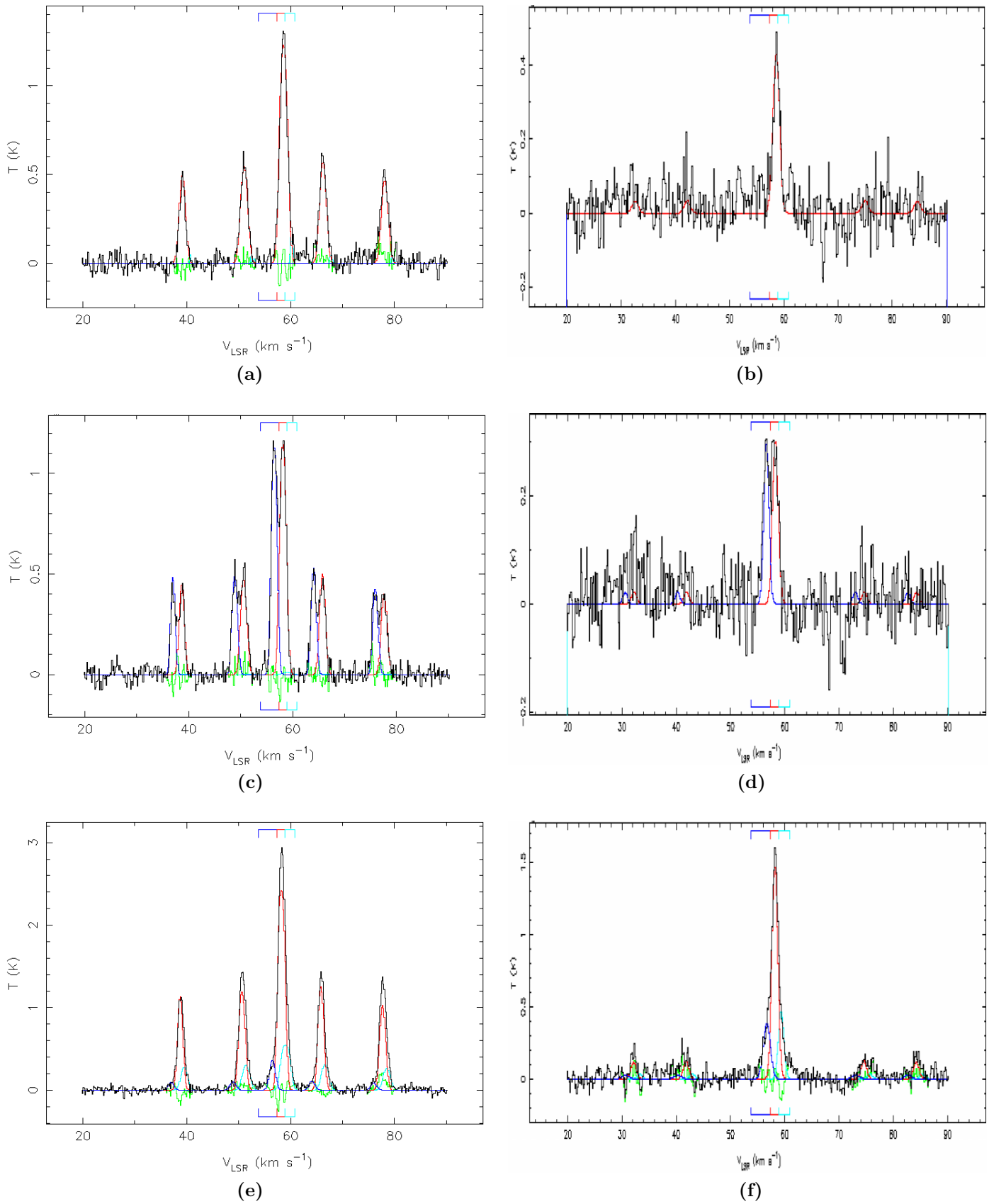

Figure 3.2: Examples of $NH_3(1,1)$ (left panels) and $NH_3(2,2)$ (right panels) spectra extracted at some selected positions for G34. The fitted velocity components are shown in blue, red, and cyan. The green line depicts the residual from the line fitting.

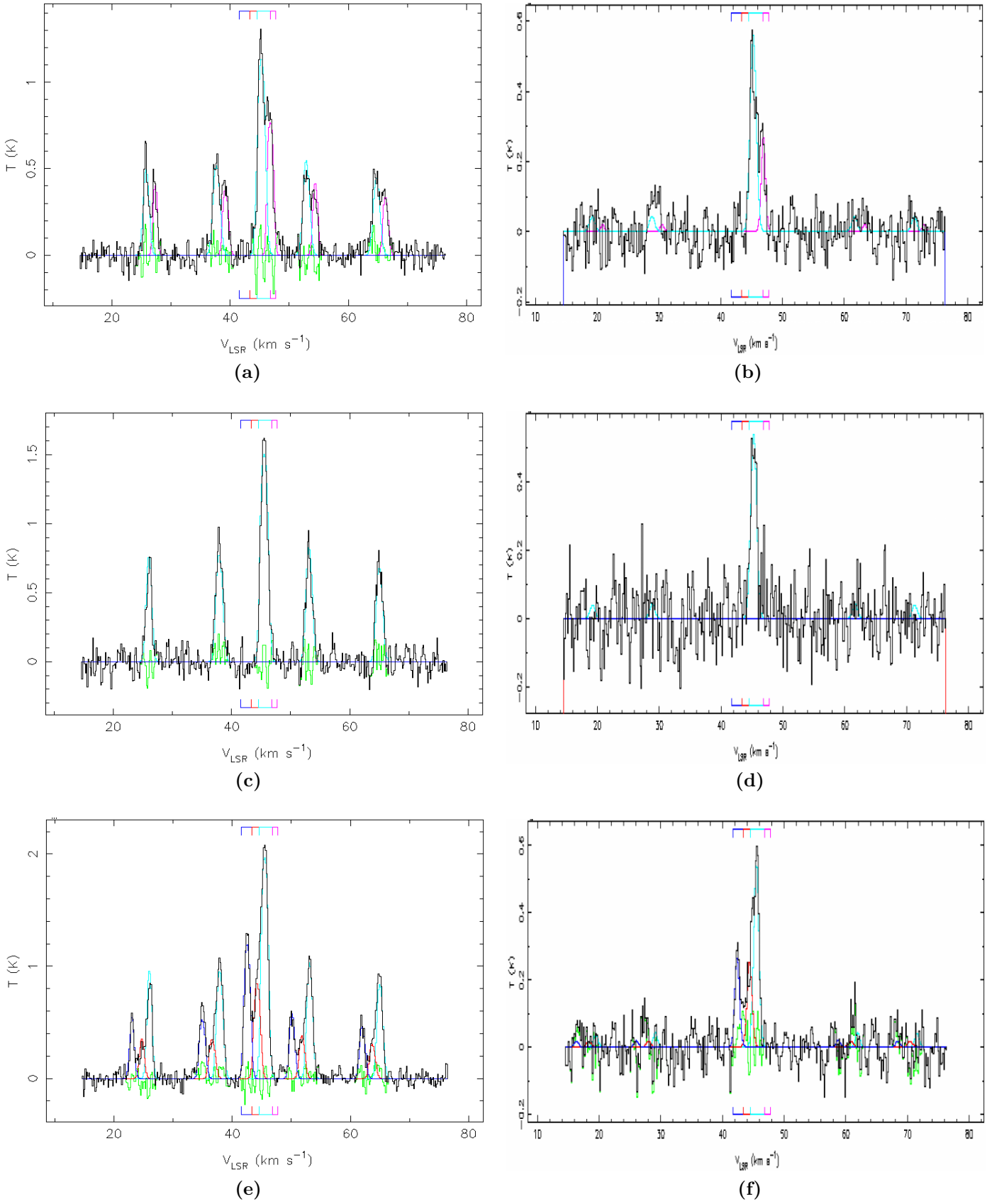

Figure 3.3: Same as in Figure 3.1 but for G35.

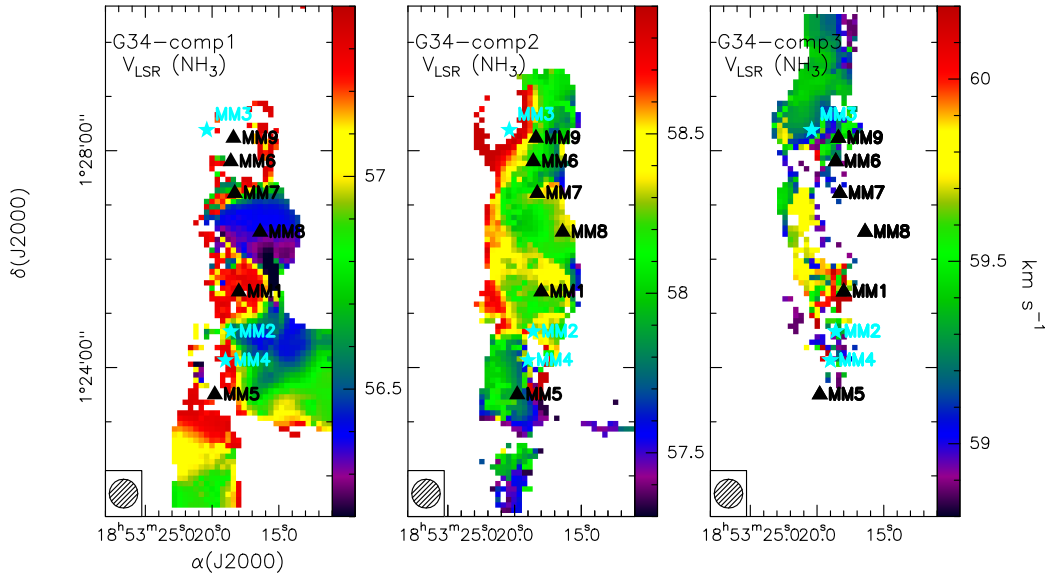

Figure 3.4: G34 central velocity component maps for components 1, 2 and 3 . Filled starred symbols refer to protostellar clump and filled triangle symbols refer to prestellar clumps.

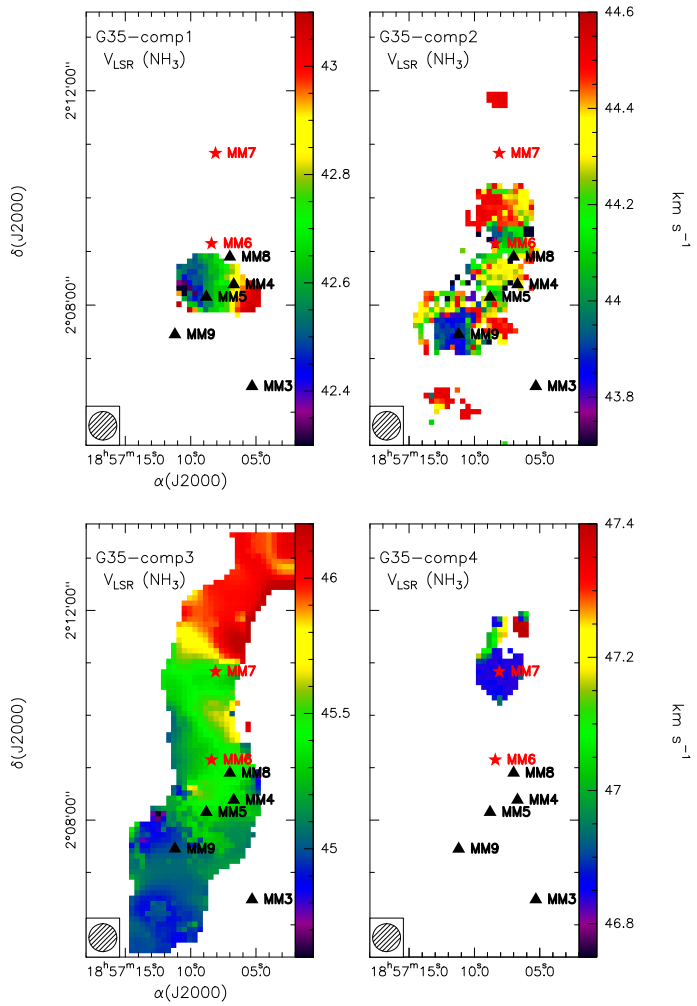

Figure 3.5: G35 central velocity component maps for components 1, 2, 3 and 4. Symbols are the same as in Figure 3.4.

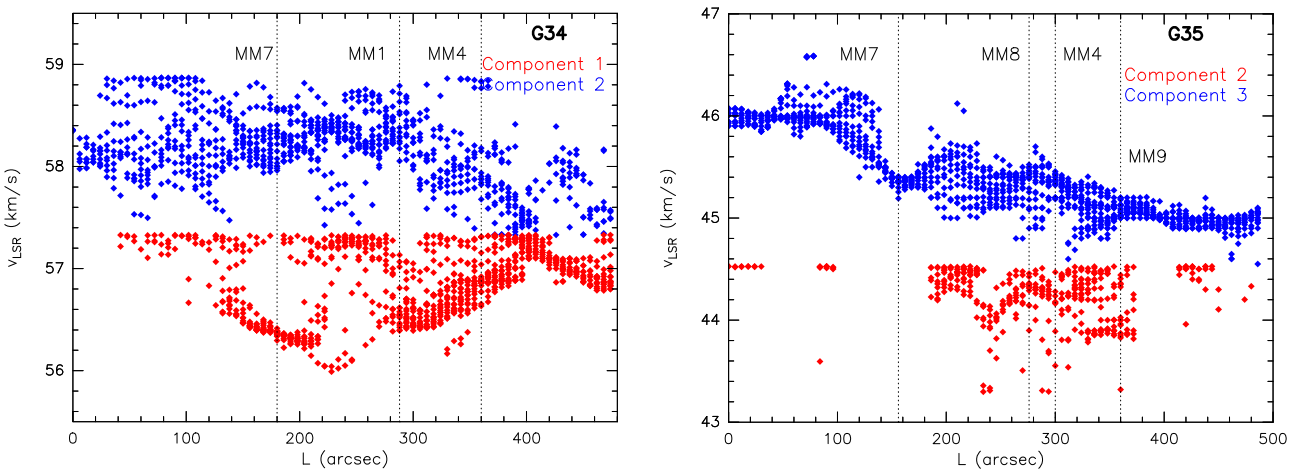

Figure 3.6: (a) Velocity vs distance plots for velocity components 1 and 2 in IRDC G34. (b) Velocity vs distance plots for velocity components 2 and 3 in IRDC G35. The locations of the millimeter clumps identified by Rathborne, Jackson and Simon (2006) are depicted with soft dashed lines in both panels by vertical dashed lines.

In the case of the central velocity maps for G35 (Figure 3.5), it is evident that not all the components have a filamentary morphology, for example, components 1 and 4 are compact. Component 1, with a size of 1.265 pc, shows a velocity gradient of 0.639 $\mathrm{km\,s^{-1}\,pc^{-1}}$ in the east-west direction. Component 2 and 3 present filamentary structure, the latter is considered as the main velocity component of the IRDC and presents an extended velocity gradient of 0.188 $\mathrm{km\,s^{-1}\,pc^{-1}}$ in the southeast-northwest direction.

In order to have a better understanding of the kinematics, central velocity vs distance plots can be seen in Figures 3.6a and 3.6b for the most filamentary components 1 (red) and 2 (blue) in G34 and for components 2 (red) and 3 (blue) in G35 respectively. The distance (in units of arcsecs) in this plots is measured from the north to the south along the length of the filaments.

From Figure 3.6a (left panel) we can clearly see that the range of central velocities for component 1 is between 56.0 and 57.4 $\mathrm{km\,s^{-1}}$ while the range for component 2 is between 57.3 and 59.9 $\mathrm{km\,s^{-1}}$. These filamentary components do not present a particularly clear gradient along the major axis, however it is possible to see that for component 2 there are some indicators of a gradient (from velocity value of 58.4 $\mathrm{km\,s^{-1}}$ at $L \sim 320$ arcsec, towards 57.4 $\mathrm{km\,s^{-1}}$ at $L \sim 480$ arcsec); also there are hints of an oscillatory pattern in the velocity for component 2, which is similar to the ones observed in earlier studies for other regions (Hacar and Tafalla 2011) and are associated with the location of the millimeter clumps, as depicted in the figure.

The behaviour for G35 seen in the plot of Figure 3.6b (right panel) is more explicit, although there is no discernable correlation for filamentary component 2; the component 3, which is the main velocity component of G35, shows an increasing slope along the distance from south to north that is related to the prominent 0.188 $\mathrm{km\,s^{-1}\,pc^{-1}}$ velocity gradient explained above (Figure 3.5), with values in velocity going from 44.8 $\mathrm{km\,s^{-1}}$ to 46.0 $\mathrm{km\,s^{-1}}$ along a length of around 423 arcsec. Again, and even more explicit, is possible to see the oscilatory behaviour, confirming its relation with the location of the millimeter

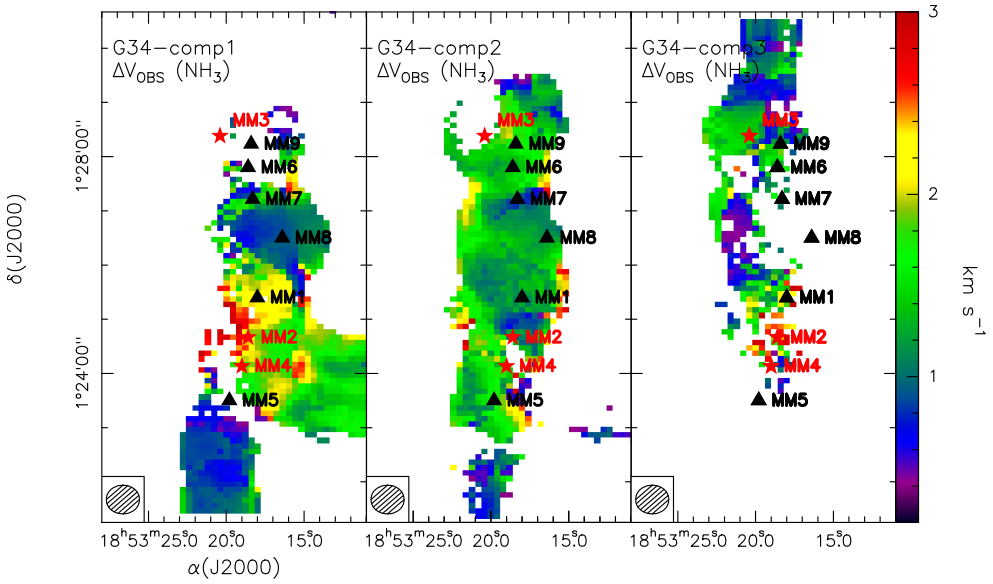

Figure 3.7: Linewidth maps for G34 velocity components 1, 2 and 3. Symbols are the same as in Figure 3.4.

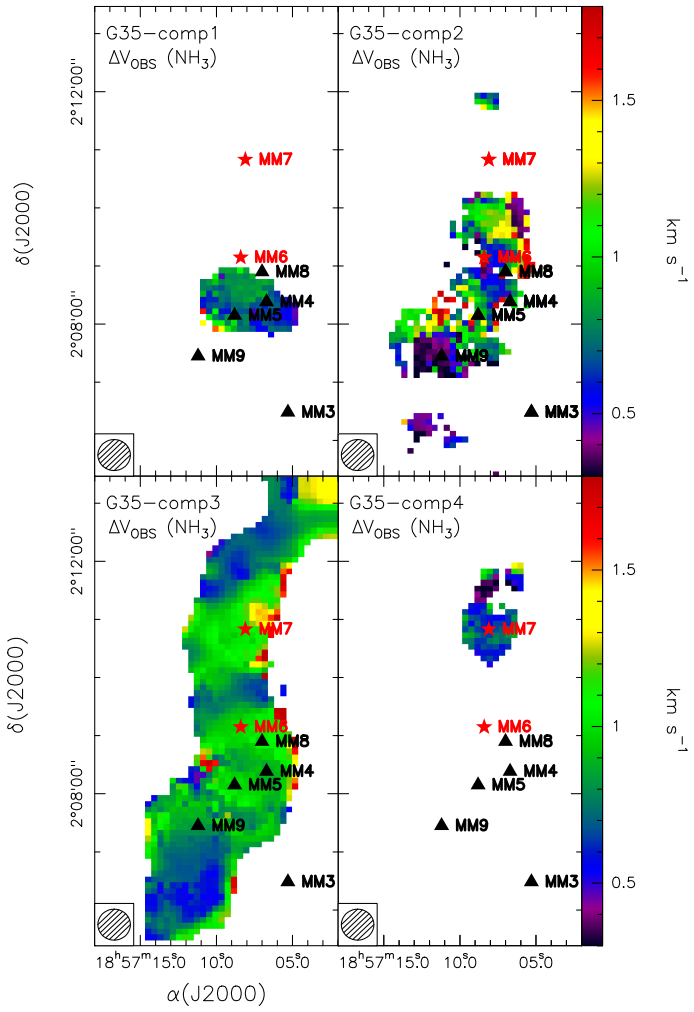

Figure 3.8: Linewidth maps for G35 velocity components 1, 2, 3 and 4. Symbols are the same as in Figure 3.4.

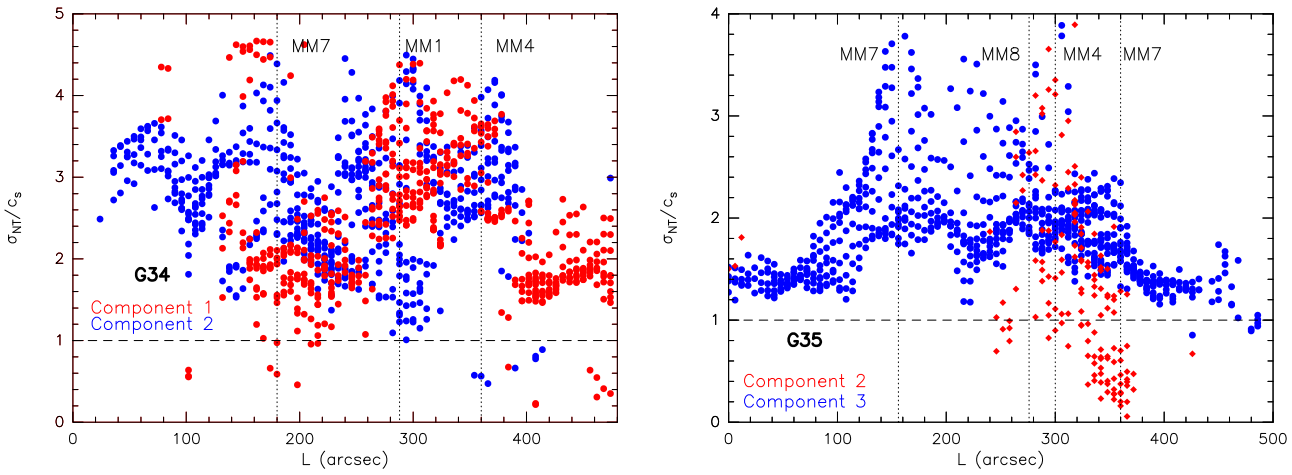

Figure 3.9: σ_{NT}/c_s vs distance plots for velocity components 1 and 2 in IRDC G34 (a), and for velocity components 2 and 3 in G35 (b). The dashed line represents a value of $\sigma_{NT}/c_s = 1$ and the location of the millimeter clumps identified by Rathborne, Jackson and Simon (2006) are represented by the vertical dashed lines.

clumps.

Linewidth maps can be also seen in Figure 3.7 for G34 and in Figure 3.8 for G35. Component 1 of G34 exhibits that the linewidth (which is related to the velocity dispersion σ_v by $\sigma_v^2 = \Delta v^2/8\ln 2$) is larger in the central part of the IRDC where it acquires values $\gtrsim 2.5\,\mathrm{km\,s^{-1}}$, also in the west part of the cloud, component 1 linewidths reach higher values.

Component 2 does not present large values in linewidth in the central part. It is also noticeable that the linewidth map for this component is quite homogeneous, with values in linewidth of around 1 - 1.6 $\mathrm{km\,s^{-1}}$. Also in component 2, it can be seen how in the edges of the map the linewidth increase, reaching values of up to 2.2 - 2.4 $\mathrm{km\,s^{-1}}$.

For G35 a similar behaviour is seen: for the main velocity component the linewidths become larger along the central part of the filament, with its values going from 0.6 $\mathrm{km\,s^{-1}}$ up to 1.4 $\mathrm{km\,s^{-1}}$; the first velocity component has no discernable variations in its velocity dispersion.

The observed linewidth is a combination of both the contribution of the thermal and the non-thermal motions of the gas. These motions, at the same time, are related mainly to turbulent effects, however rotation motions along with inflow motions or even additional unresolved velocity components may also contribute to it.

In order to estimate the non-thermal velocity dispersion, we used the observed linewidth to sustract the thermal component. Detailes of this procedure are given in Table 3.3. Figure 3.9 shows the distribution of the non-thermal velocity dispersion component as a function of postion along the filamentary components of G34 (left panel) and G35 (right panel).

For G34 we can see that both components show large dispersion with some trend to wavelike features along the filament length for both velocity components. Most of the

pixel points in the regions are above the value $\sigma_{\rm NT}/c_s = 1$ which indicates that the NH_3 gas motions in the region are mainly supersonic. It is possible to see that the highest values of $\sigma_{\rm NT}/c_s$ coincide with the positions of clumps MM1, MM4 and MM7 (see Figure 3.9 left panel), a tendency also studied in Hacar and Tafalla (2011).

Something similar occurs for the IRDC G35. For example component 2, located between 240 and 440 arcsec, shows a large range of values of $\sigma_{\rm NT}/c_s$, with plenty of pixels presenting subsonic gas motions, and some pixels exceeding the sonic limit, with values up to 4. But the clearest sign of supersonic motions for the dense gas in the region is given by the points plotted for velocity component 3, most of which exceed the limit of $\sigma_{\rm NT}/c_s = 1$, exhibiting also an oscillatory feature with peaked values at $L \sim 160$ arcsecs and $L \sim 305$ arcsecs, which coincide with the millimeter clumps MM7 and MM4 respectively, as can be seen in Figure 3.9 right panel where they are represented by the vertical dashed lines.

The mean values of the total velocity dispersion $\sigma_{\rm TOT}$ and the non thermal component of the dispersion $\sigma_{\rm NT}$ are listed for the filamentary components of each IRDC in Table 3.2, along with mean values of the coeficient $\sigma_{\rm NT}/c_s$.

From this point forwards all maps and figures will be related to the filamentary components of G34 and G35, although when needed, reference to the more compact components will be also given. Table 3.2 shows the physical parameters derived from NH_3 for each one of the identified velocity components.

3.2.3 Column Density and Rotational Temperature

The column density maps of NH_3 for each component are presented in Figure 3.10. To obtain the $N(NH_3)$ we assumed that there are uniform excitation conditions for all the hyperfine components of $NH_3(1,1)$ and a beam filling factor equal to one.

Components 1 and 2 for G34 (Figure 3.10 upper panels) evidence sites of high column densities at both the northwest part of the cloud and in the south. We immediatly see that the peaks in NH_3 column density mainly coincide with the millimeter clumps identified by Rathborne, Jackson and Simon (2006).

Something similar occurs in component 3 for G35 (Figure 3.10 lower panels) where the higher NH_3 column density sites are directly corresponded with most of the millimeter clumps. Component 2 escapes this behaviour, having relatively low column densities in comparison with the main filament: most of it is between the range of $1 - 5 \times 10^{14}\,{\rm cm}^{-2}$.

The maps with the rotational temperature are seen in Figure 3.11, the upper panels show the configuration for G34 filamentary components while the lower panels exhibit the behaviour of rotational temperature for the components of G35. The range of values of rotational temperature determined for G34 and G35 are around 12 – 27 K and 9.5 – 14.5 K respectively.

In G34, it is noticed that for component 1 the rotational temperature increases towards the east of MM1 and that for filamentary component 2 there is also an increment in temperature, of up to 25 K towards the clumps MM2 and MM4 identified by Rathborne, Jackson and Simon (2006).

For filament G35, an overall analysis allows us to find that the values in rotational temperature are higher for component 2 than for the main component 3. The main filament has a $T_{\rm rot} \sim 11$ K with some local spots where the temperature is relatively higher, rea-

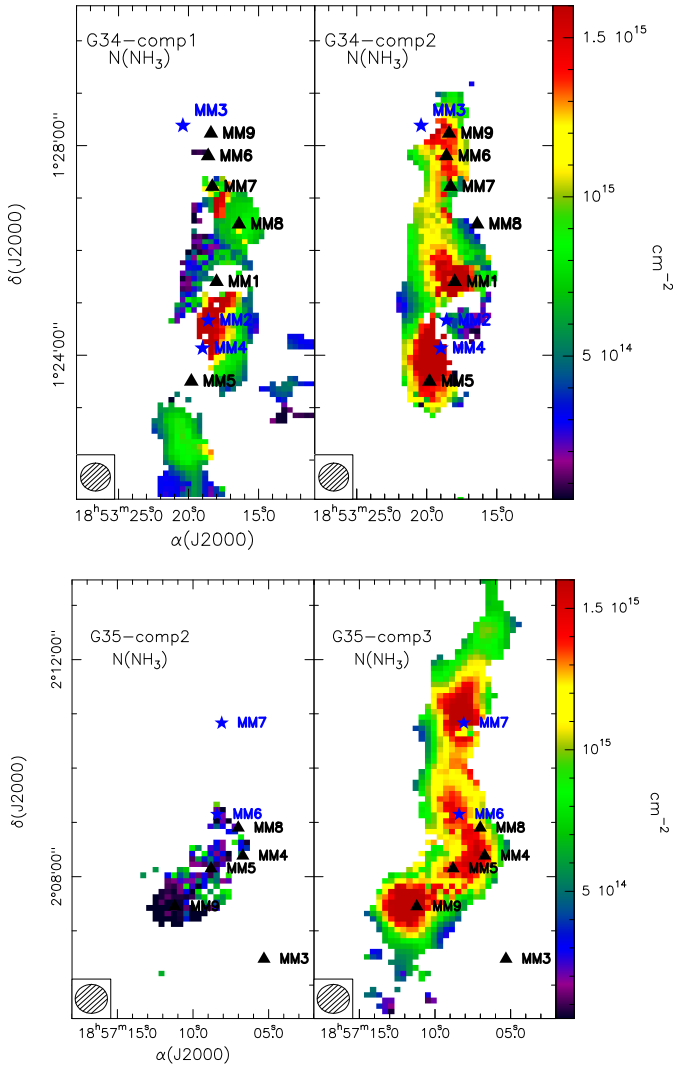

Figure 3.10: Column density maps for G34 filamentary velocity components 1 and 2 (upper panels) and for G35 filamentary velocity components 2 and 3 (lower panels). Symbols are the same as in Figure 3.4.

ching values of 13 K. Unlike G34, there is no discernable local rotational temperature enhancements that can be directly related to the protostellar clumps.

The results summarizing both the compact and filamentary velocity components are reported in Table 3.2.

3.2.4 Mass and Mass per Unit Length

Mass calculations are provided in Table 3.3 for the filament components of both regions. The mass of each region was computed as:

$$M = \frac{\sum_i N_i \Delta s m_{\mathrm{H_2}}}{X\,(\mathrm{NH_3})} \tag{3.1}$$

where $\sum_i N_i$ is the sum of NH_3 column densities of all pixels in cm^{-2}, Δs is the area in cm^2 of one pixel, m_{H_2} is the mean molecular mass of the interstellar gas per molecule of

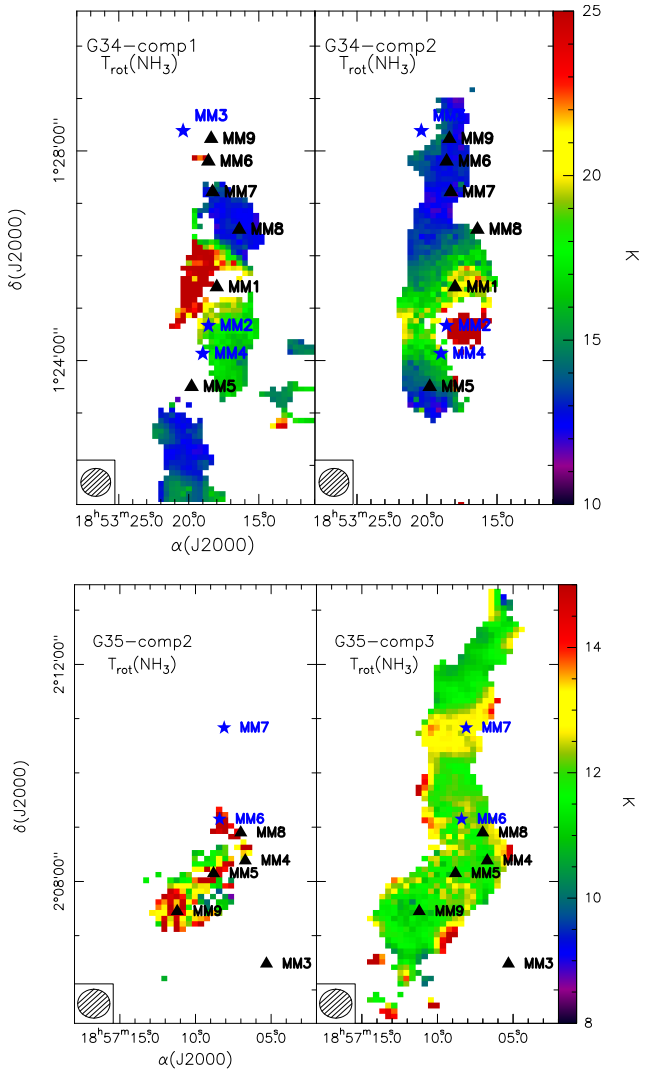

Figure 3.11: Rotational Temperature maps for G34 velocity components 1 and 2 (upper panels) and for G35 velocity components 2 and 3 (lower panels). Symbols are the same as in Figure 3.4.

TABLE 3.2: SUMMARY OF THE PHYSICAL PARAMETERS DERIVED FROM NH_3

Region	Comp[a]	Shape	$v_{\rm LSR}$ $\left(\mathrm{km\,s^{-1}}\right)$	$\Delta v_{\rm obs}$ $\left(\mathrm{km\,s^{-1}}\right)$	τ_m	$N\,(NH_3)$ $\left(\times 10^{15}\,\mathrm{cm^{-2}}\right)$	$T_{\rm rot}$ (K)
G034.43+00.24	1	Filamentary	56.84 ± 0.03	1.447 ± 0.239	1.441 ± 0.616	0.733 ± 0.200	17.01 ± 1.09
	2	Filamentary	58.18 ± 0.05	1.375 ± 0.211	2.089 ± 0.992	1.066 ± 0.218	16.12 ± 1.20
	3	Compact	59.42 ± 0.05	1.219 ± 0.223	1.835 ± 0.858	0.549 ± 0.216	22.46 ± 5.12
G035.39-00.3	1	Compact	42.70 ± 0.06	0.752 ± 0.172	1.855 ± 0.437	0.593 ± 0.042	12.18 ± 3.46
	2	Filamentary	44.25 ± 0.06	0.817 ± 0.208	1.969 ± 0.829	0.282 ± 0.107	17.06 ± 5.47
	3	Filamentary	45.41 ± 0.04	0.895 ± 0.205	2.562 ± 0.366	1.074 ± 0.238	12.02 ± 1.04
	4	Compact	46.97 ± 0.01	0.651 ± 0.219	2.895 ± 0.582	0.729 ± 0.283	12.45 ± 2.06

[a]The values of the parameters for each component are mean values, averaged over all the pixels with emission shown in the maps appearing in this chapter.

TABLE 3.3: SUMMARY OF FILAMENT PROPERTIES

Comp ID	$\sigma_{\rm TOT}$ [a] $\left(\mathrm{km\,s^{-1}}\right)$	$\sigma_{\rm th}$ [b] $\left(\mathrm{km\,s^{-1}}\right)$	$\sigma_{\rm NT}/c_s$ [c]	$T_{\rm k}$ [d] (K)	M [e] $\left(\mathrm{M_\odot}\right)$	M/L $\left(\mathrm{M_\odot\,pc^{-1}}\right)$	$(M/L)_{\rm crit}$ [f] $\left(\mathrm{M_\odot\,pc^{-1}}\right)$	α_v [g]
G034.43+00.24								
1	0.659 ± 0.098	0.100 ± 0.084	2.360 ± 0.645	20.80 ± 3.49	584 ± 1	163 ± 0.3	202 ± 60	1.20
2	0.667 ± 0.099	0.096 ± 0.065	2.480 ± 0.619	18.93 ± 2.60	974 ± 1	272 ± 0.3	207 ± 61	0.80
G035.39-00.3								
2	0.416 ± 0.131	0.097 ± 0.011	1.349 ± 0.190	19.21 ± 4.49	311 ± 13	115 ± 2	80 ± 50	0.70
3	0.416 ± 0.078	0.079 ± 0.016	1.829 ± 0.124	12.75 ± 2.58	6129 ± 14	897 ± 2	80 ± 30	0.09

[a]The total velocity dispersion $\sigma_{\rm TOT}$ was obtained through the expression:

$$\sigma_{\rm TOT} = \frac{\Delta v}{(8 \ln 2)^{1/2}}$$

[b]The thermal component of the velocity dispersion was calculated using

$$\sigma_{\rm th} = \left(\frac{k_B T_k}{\mu m_H}\right)$$

where k_B is the Boltzmann constant, T_k is the kinetic temperature, μ is the mean molecular mass of the gas and m_H is the mass of the hydrogen atom.

[c]The non thermal component of the velocity dispersion is computed from the quadrature expression

$$\sigma_{\rm NT} = \left(\sigma^2_{\rm TOT} - \sigma^2_{\rm Th}\right)^{1/2}$$

meanwhile the expression for the sound speed c_s is similar to the equation for the thermal component but using the molecular hydrogen mean molecular mass instead of that from the gas.

[d]Related to the rotational temperature expression used in Estalella 2017

$$T_{\rm rot} = \frac{T_k}{1 + \frac{T_k}{T_0} \ln\left[1 + 0.73 e^{-(E_{21} - E_{22})/k T_k}\right]}$$

with $T_0 = 40.99\,\mathrm{K}$, $(E_{21} - E_{22})/k = 16.26$ K.

[e]Calculated using abundances of 3.0×10^{-8} for G34 (Pillai et al. 2006) and 2.1×10^{-8} for G35 (Sokolov et al. 2017) respectively.

[f]Calculated as

$$(M/L)_{\rm crit} = \frac{2\sigma^2_{\rm TOT}}{G}$$

[g]Mass per unit length virial parameter (see text).

H_2 calculated as $m_{H_2} \sim 2.8 m_{\rm H}$ with m_H being the hydrogen mass, and $X\,(NH_3)$ is the abundance of ammonia with respect to molecular hydrogen for each region. For G35 we adopted the ammonia abundance derived recently by Sokolov et al. (2017) of 2.1×10^{-8}, while for G34 we used 3.0×10^{-8} since it is the average value obtained by Pillai et al. (2006) toward a sample of IRDCs.

In the case of G34 the mass values vary between the two components, despite sharing a similar area, which indicates a difference in the NH_3 column desity between components 1 and 2; mass calculations give $584\,\mathrm{M_\odot}$ for component 1 and $974\,\mathrm{M_\odot}$ for component 2. Calculations for the compact component 3 were also made, resulting in a mass contri-

bution of around 181 $M_\odot$, which is, as expected, the lowest mass value among the three components (see Table 3.3).

As for G35, the mass of the main component is larger than for the second velocity component subfilament by one order of magnitude, with values of 6129 $M_\odot$ and 311 $M_\odot$ respectively. The difference with respect to the main component became obvious when calculations for mass in the compact components were obtained, resulting in 171 $M_\odot$ and 44 $M_\odot$ for velocity components 1 and 4 accordingly.

In Table 3.3 we also list the values of the mass per unit length and the critical mass per unit length which gives an understanding of the stability of the region, a subject left for further discussion in the next chapter (see subsection 4.1.2).

4 Discussion and Conclusions

4.1 Discussion

In this chapter we will discuss the general results presented in Chapter 3, by analysing the density structure of the total hydrogen column density and analysing the stability of both regions. We will also discuss our results in the framework of previous studies conducted towards both low-mass and high-mass star-forming regions.

4.1.1 Radial Density Profiles

Using the NH_3 column density maps presented in Figure 3.10, we analyze the radial hydrogen column density profile for filamentary components 2 in G34 and 3 in G35. The abundances used for obtaining the molecular hydrogen column density data were of 3.0×10^{-8} for G34 (Pillai et al. 2006) and 2.1×10^{-8} in the case of G35 (Sokolov et al. 2017).

The density profiles were computed as follows: At a fixed declination, we extracted the radial density profiles from the NH3 column density maps at some selected NH_3 peaks. Finally, the NH_3 column density values were converted into H_2 column densities using the abundances mentioned earlier for the respective IRDC.

For G34 component 1 we chose two spots at declination coordiantes 01°25´23.3″ in the middle-northern part of the cloud, almost coincident with the position of millimeter clump MM1; and 01°24´05.3″ in the southern part, close to the position of clumps MM4 and MM5. In the case of G35 we have chosen three peaks at different declinations, one at 02°10´56.0″ in the northern part, close to the position of MM7; other at 02°08´24.2″ in the middle part, almost coincident with location of clumps MM6 and MM8 and the last one at 02°07´38.7″ which is in the southern region, very close to MM9. The locations chosen for the NH_3 column density peaks can be seen in Figure 4.1, where the dashed lines are representing the radial cuts performed in order to obtain the density profiles.

The resulting radial density profiles for both G34 and G35 are displayed in Figure 4.2. Different colors indicate different cuts in the column density map. In both cases the black continuum line is the best fit result for generated data following the density profile model for an *isothermal cylinder* described in early works by Stodólkiewicz (1963) and Ostriker (1964) and used in more recent works (e.g. Hacar et al. 2013), given by:

$$n(r) = \frac{n_\circ}{\left(1 + (r/H)^2\right)^2} \tag{4.1}$$

after some calculations an expression for the column density can be obtained

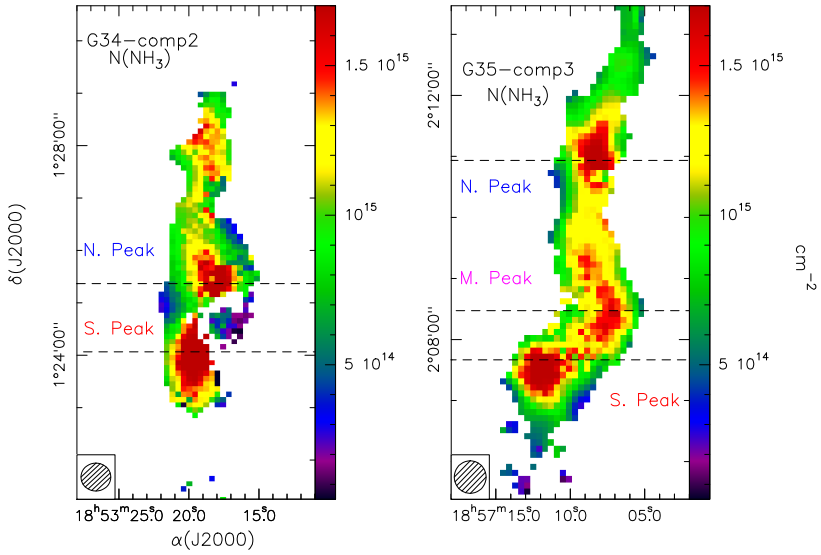

Figure 4.1: Ammonia column density maps for both G34 component 2 and G35 component 3 depicting, with the dashed horizontal lines, the cuts used to extract the radial density profile in each region.

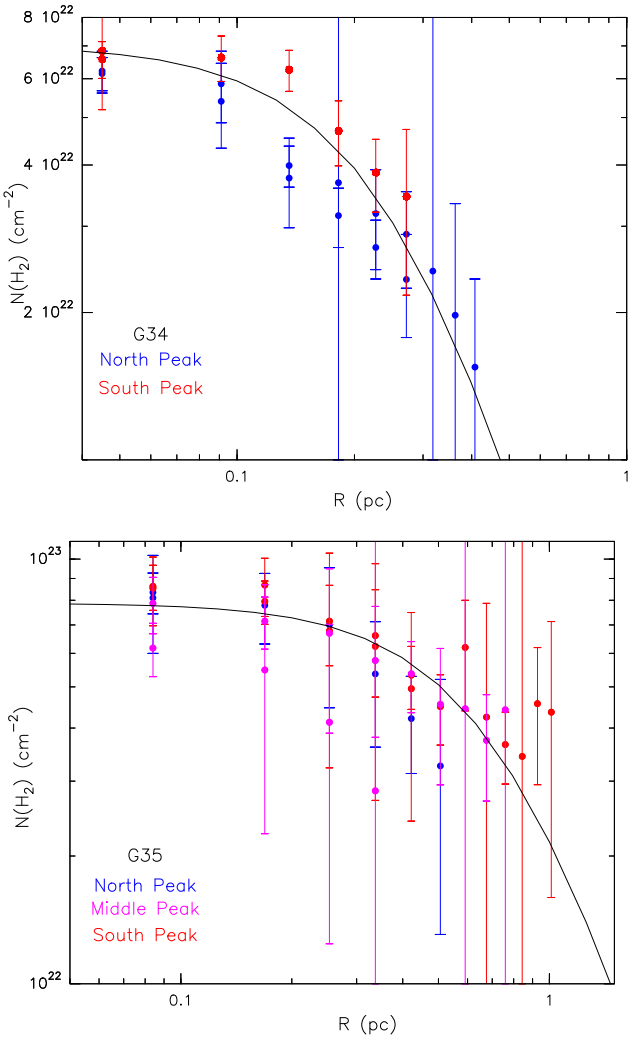

Figure 4.2: Radial column density profile for G34 (top panel) and G35 (bottom panel)

TABLE 4.1: ISOTHERMAL CYLINDER MODEL PARAMETERS

IRDC	Comp	$c_{\rm eff}$ $\left(\mathrm{km\,s^{-1}}\right)$	$\Delta v_{\rm model}$ $\left(\mathrm{km\,s^{-1}}\right)$	H (pc)	n_0 $\left(\times 10^4\,\mathrm{cm^{-3}}\right)$
G34	1	1.41	0.52	0.291	4.98
G35	3	2.36	1.19	0.854	1.96

$$N(r) = \frac{\pi}{2} n_\circ H \left(1 + (r/H)^2\right)^{-3/2} \tag{4.2}$$

with

$$H^2 = \frac{2c_s^2}{\pi G \mu n_\circ} \tag{4.3}$$

where $n_\circ$ is the central density, H is the characteristic radius of the filament obtained when $n(H) = n_0/16$, r is the cylindrical radius, c_s the isothermal sound speed, G is the grvitational constant and μ is the mean molecular mass of the gas. This is a particular case of a more general model of a power-law density profile with a flattening central density.

The isothermal cylinder model in Figure 4.2 is in good agreement with the observed density profile; the model has one free parameter, the central density n_0, which value, from the fitted model is 4.98×10^4 cm^{-3} for G34 and $1.96 \times 10^4\,\mathrm{cm^3}$ for G35. Also the fitted model allows one to calculate the linewidth nedded to support the filament against gravitational collapse, resulting in values of 0.52 km s^{-1} for G34 and 1.19 km s^{-1} for G35 with effective sound speeds of 1.41 and 2.36 km s^{-1} respectively; these parameters are listed in Table 4.1.

Depite the fact that the observed linewidth values shown in Table 3.2 are bigger than the linewidths estimated from the fitting of the isothermal cylinder model, this difference can be taken to be little within the errors of the observed estimations since the linewidth for component 2 of G34 is $1.37 \pm 0.21\,\mathrm{km\,s^{-1}}$ and for component 3 of G35 is $0.89 \pm 0.20\,\mathrm{km\,s^{-1}}$ and therefore we can say that the difference between observed and estimated linewidths is negligible.

4.1.2 Stability of Filaments

The stability of G34 and G35 can be studied by comparing the *critical* mass per unit length with the observed mass per unit length (see Table 3.3). We can use as a reference the virial parameter to predict the stability of the dense gas for the filamentary velocity components (e.g. Bertoldi and McKee 1992; Busquet et al. 2013; Kauffmann, Pillai and Goldsmith 2013):

$$\alpha_v = \frac{(M/L)_{\rm crit}}{(M/L)} \tag{4.4}$$

For a virial parameter with values $\alpha_v \simeq 1$, the estimation indicates that the filamentary components of dense gas are close to virial equilibrium. However, virial parameters with $\alpha_v \lesssim 2$ indicate supercritical regions, which are bound or marginally gravitationally bound and might undergo collapse when perturbed; the counter case refers to subcritical regions, regions that are unbound and may expand themselves and dissolve back into the diffuse interstellar medium.

Using the values listed in Table 3.3 for M/L and $(M/L)_{\rm crit}$ we find that for components 1 and 2 of IRDC G34 the values for the virial parameter are 1.2 and 0.8 respectively; meanwhile for IRDC G35 the respective values for componets 2 and 3 are 0.7 and 0.09.

As can be noted, for filamentary velocity components 1 and 2 in G34 and for component 2 in G35 the values of the virial parameter are closed to 1, indicating that they are near virial equilibrium; however, all of the values are $\lesssim 2$ so the dense gas presents instabilities and it would ultimately collapse, and the clouds could even undergo fragmentation.

This is currently in agreement with the topic discussed in the last section, where through the fitting of the isothermal cylinder model for the density profiles, it was found that the linewidths needed to preven the filament from collapsing are slightly different for the mean values obtained from the results, therefore one can say that both regions have instabilities appreciated from analysing the most filamentary velocity components.

Furthermore, the presence of an instability could also be hinted by analysing the motions obtained from the σ_{NT}/c_s vs distance plots in Figure 3.6, where we found that most of the dense gas traced for the filamentary components of both clouds are going through supersonic motions, that could be related with the presence of turbulent motions.

The above stability calculation has been estimated in other works in the same regions using different tracers. For example Foster et al. (2014) use multi-wavelength dust emission observations and obtained that the majority of the IRDC G34, with the exception of the ends of the filament, is globally bound and will probably collapse. Although it is a different approach since in our work we analyzed the stability of the velocity components, other works (e.g. Xu et al. 2016 using ^{13}CO and C^{18}O) find similar values between the $(M/L)_{\rm crit}$ and the observed (M/L) for the total region, however, the latter is smaller so the authors argue that although it should collapse the precense of turbulent motions might be helping in stabilizing the filament.

This calculations indicates that the observed mass per unit length for component 3 of G35 is large (see Table 3.3); this can be explained by the fact that this is the main velocity component obtained for G35 and that it represents a great portion of the total mass of the cloud.

Recent work by Sokolov et al. (2017) also using ammonia data, find lower masses than the ones obtained in the present work for G35, however they use a different approach in the calculation of the mass since they use data of column desities provided by *Herschel,* different from our calculations that rely in the abundance factor. Moreover they calculate a range for the critical line masses that is between 50 and 200 $\mathrm{M}_\odot\,\mathrm{pc}^{-1}$ which is in agreement with the values obtained for the filamentary velocity components of this IRDC in the present work (see Table 3.3).

4.1.3 Comparison with Filamentary Regions of Low-Mass Star Formation

For the pusposes of further analisys it is interesting to compare the behaviour of the two IRDCs filaments with those regions where low-mass star formation is taking place.

Arzoumanian et al. (2011) analize the density profiles for 27 filaments in the IC5146 molecular cloud based on results from the *Herschel Gould Belt* survey. They fit the idealized model of the isothermal cylinder, following the exact same pattern: at large radii from the peak in column density, the behaviour of the model is that of a power law, however, *none* of the filaments follow a behaviour completely similar to the model described in Ostriker (1964) which has a power of 1.5, and moreover the filaments are found to follow a power law with a power index value between 0.5 and less than 1.5. Density profiles are also studied in L1517 through dense gas tracer such as N_2H^+ in Hacar and Tafalla (2011), where for their four filament complex a range of $0.3 - 1.0{\times}10^4\,\mathrm{cm}^{-3}$ for central densities which compare to the values seen in Table 4.1 in which the central densities found for G34 and G35 are of the order of $\sim 10^4\,\mathrm{cm}^{-3}$.

Several authors also derived the mass per unit length and the corresponding critical mass per unit length in order to study stability properties. Arzoumanian et al. (2011) find that as the case for IRDCs G34 and G35, 8 out of 27 filaments present gravitational instabilities for IC5146. The ranges of mass per unit length obtained for these filaments are from as little as 1 $\mathrm{M}_\odot\,\mathrm{pc}^{-1}$ to the highest value of 152 $\mathrm{M}_\odot\,\mathrm{pc}^{-1}$, since these *Herschel* filaments have column densities that range from 0.57×10^{21} to $7.5 \times 10^{21}\,\mathrm{cm}^{-2}$, contrasting with the values obtained for G34 and G35 where the column density values were of the order of around $10^{22}\,\mathrm{cm}^{-2}$, also IC5146 is a low-mass star-forming region justifying their lower mass per unit length values. Mass per unit length are also studied for B213 in Taurus in Hacar et al. (2013) using N_2H^+ and $C^{18}O$, where the authors conclude that the typical value is $M/L \sim 15$ for the resolved filaments, evidencing that for low mass star-forming regions is expected that values of such a parameter are lower than the ones obtained for high-mass star forming regions such as G34 and G35.

G34 and G35 are found to be both supercritical since the values of the virial parameter are below 2 in both filaments, this is another difference, since when comparing the results obtained by Benedettini et al. (2015) in the Lupus region subfilaments, it is found that most of them are subcritical.

When refering to the dense gas filament length, one can compare with what was obtained in the low-mass star forming regions such as the Taurus region (Hacar and Tafalla 2011). The length of the filaments studied in the Taurus L1517 cloud is of around 0.5 pc, a similar length scale as the one shown in filaments of B213 (Hacar et al. 2013) which is uncomparable with the found lenghts of 3.6 and 6.8 pc for G34 and G35; this may be also in part because the scales used in our work (beam 32" with a spatial scale of 0.3 pc) and the works used in the low-mass star forming region of Taurus region (beam 56" with a spatial scale 0.038 pc) are different. This might imply that both Hacar and Tafalla (2011) and Hacar et al. (2013) are able to resolve substructures that we are unable to.

The general behaviour of the motions of the gas for filaments in the dark cloud L1517 is quiescent: similar plots as the ones shown in Figure 3.9 which show the behaviour of σ_{NT}/c_s against distance along the filament length predict that instead of being mostly supersonic, the gas traced for these filaments in this low-mass star forming region are

subsonic or sonic. This seems to be an apparent general difference between regions such as the massive IRDCs G34 and G35 with sites of low-mass star formation, since the behaviour of showing sonic-subsonic motions is also repeated for the filamentary Musca cloud (Hacar et al. 2016), where although some movements are above the limit $\sigma_{NT}/c_s = 1$ up to values of 2.5, these are uncomparable with the values shown for G34 and G35 where most of the ammonia dense gas traced along the filaments is $\sigma_{NT}/c_s \geq 2$.

One can also compare the kinematics of the different regions through the value of both the global and local gradients. The values of the gradients for G34 and G35 range from 0.188 to 1.854 $\mathrm{km\,s^{-1}\,pc^{-1}}$ (see Table 3.2); this range is in good agreement with the local gradients found in regions such as Taurus for L1517 with values in different filaments within 0.9 to 1.4 $\mathrm{km\,s^{-1}\,pc^{-1}}$ (Hacar and Tafalla 2011) and for the Musca filament within values of 0.2 to 0.3 $\mathrm{km\,s^{-1}\,pc^{-1}}$ (Hacar et al. 2016).

Another similarity is present when analysing the behaviour of the central velocity of the filaments with the distance along their length; it was found in Chapter 3 that both G34 and G35 filamentary velocity components show an oscillatory tendency along the distance, such a behaviour is repeated in other works where the same plots are computed such as the ones analying the L1517 filaments (Hacar and Tafalla 2011) and the Musca cloud (Hacar et al. 2016). Such oscillatory pattern seen in these gradient plots is related to the positions of the most prominent cores or clumps in such regions, this is confirmed by Figure 3.6 where for both IRDCs the behaviour along the length of the filament is evident and influenced by the millimeter clumps identified in Rathborne, Jackson and Simon (2006).

Hacar and Tafalla (2011) established through a simple kinematic model that the oscillatory pattern is consistent with core-forming motions along the axis of the filaments. A model similar to this could be used on G34 and G35, however a more detailed study is needed, and can be left for a future work.

In general one could say that, as expected, the properties shown in regions of low-mass star formation such as filaments in IC 5146, Taurus (dark cloud L1517 and B213), the Lupus region and in the Musca cloud are very different from those found for G34 and G35, for example when comparing the density profile power law index, their stability behaviour since low mass star forming regions tend to be subcritical, the size and mass ranges. However, they exhibit similarities when comparing the kinematics through their global and local velocity gradients, and also show similar behaviour when analysing how their central velocities change with distance along the filaments.

4.1.4 Comparison with Filamentary Regions of High Mass Star Formation

There are little number of works regarding the analysis of the properties of filaments in high-mass star-forming regions specially using spectroscopic information, with both high and low mass density tracers (e.g. Schneider et al. 2010; Busquet et al. 2013; Henshaw et al. 2014; Hacar et al. 2017; Sokolov et al. 2017). These studies in high-mass star forming regions have concluding remarks about several properties such as the kinematics, the stability and the temperature of the filaments.

For analysing the properties of the gas concerning this kind of regions we will mainly refer to Busquet et al. (2013), where several filaments in the IRDC G14.225–0.506 (hereafter

G14) are analysed extensively. Busquet et al. (2013) work is of much interest for comparison with the G34 and G35 since it shares a number of similarities with the present work, like the NH_3 tracer used for observations. Another important similarity between G34, G35 and G14 is that all of them are nearby clouds, with kinematic distances of 1.56, 2.9 and 1.98 kpc respectively.

In the work describing G14 Busquet et al. (2013) obtained values of the total velocity dispersion ($\sigma_{\rm TOT}$) are quite similar to the ones found for the filamentary velocity components in IRDCs G34 and G35. For example, their range of values in total velocity dispersion is 0.49 - 1.09 $\mathrm{km\,s^{-1}}$ while the obtained ranges for both G34 and G35 is 0.42 - 0.67 $\mathrm{km\,s^{-1}}$ which are in the same order of magnitude.

One can go a step further into analysing the nature of the motions of the dense gas inside these regions. We have found in Chapter 3 that most of the motions present in both G34 and G35 are supersonic, related to the presence of turbulence, with $\sigma_{NT}/c_s > 1$ and ranging from 1.35 - 2.48. This is in good agreement with the kind of motions of the network of filaments in Busquet et al. (2013) since they are found to be also mostly supersonic, with σ_{NT}/c_s ranging between 2 and 5; these supersonic motions in high mass star-forming regions (e.g. Schneider et al. 2010; Jiménez-Serra et al. 2010) seems to be a tendency and clashes with the found sonic and subsonic motions in low mass star-forming locations.

When comparing with the analysis of the gas motions as a function of the distance described in Hacar et al. (2017) for the Orion A filament region, they find changes in linewidth of up to 2.5 – 3.0 $\mathrm{km\,s^{-1}}$ which are explained by increments in temperature, however such a steep change in linewidth is absent when observing all the components of G34 and G35 where the value range is 0.65 – 1.45 $\mathrm{km\,s^{-1}}$.

G34 and G35 are very massive objects, as can be seen in Table 3.3 for the mass values obtained with the ammonia tracer for the filamentary components is between ∼300 - 6000 $M_\odot$. The stability of these high-mass star formation regions is also comparable with the results obtain for our two IRDCs, which predict them to be unstable.

The network of filaments of G14 studied in Busquet et al. (2013) present a similar behaviour, comparison between the observed mass per unit length and the virial mass per unit length leads to determining that most of the filaments are supercritical with virial parameters $\alpha_v \lesssim 2$ just as happens for G34 and G35.

Rotational temperatures are also analysed in these studies, specifically for G14, Busquet et al. (2013) using the ammonia tracer found values are in the range of 10 - 16 K; this is therefore another characteristic which is very similar when compared with the resulted mean rotational temperature acquired for G34 and G35 from the velocity component fitted spectra which shows a range of ∼12 - 22 K (see Table 3.3).

Finally, the kinematics of the gas present in these regions can be studied by, for example, comparing the gradients obtained for the Orion A filament by Hacar et al. (2017) when studying the collapse motions occurring in the OMC-1 region through CO isotopologs with the ones observed for G34 and G35; it presents a global velocity north-south gradient of $\leq 1\,\mathrm{km\,s^{-1}\,pc^{-1}}$ which is in good agreement with the one present in the main component of G35 that has a value of 0.188 $\mathrm{km\,s^{-1}\,pc^{-1}}$. Also, the Orion A filament, much like the components of G34 and G35, exhibit local gradients of higher values $> 1\ \mathrm{km\,s^{-1}\,pc^{-1}}$, that in Hacar et al. (2017) are related to the collapse motions.

In general, both results for IRDCs G34 and G35 agree with the results obtained by other authors when analysing filaments in regions of high-mass star formation.

4.1.5 Further Discussion

Both IRDCs have been widely studied with special attention paid to their kinematics and dynamical characteristics. They both exhibit multiple velocity components which might be related to different substructures behaving independently. This is a tyical characteristic of filamentary IRDCs, they are composed of diferent subfilaments as mentioned in André et al. (2014).

G34 has been studied with different tracers other than ammonia: emission in $C^{18}O$ (1–0) (e.g. Xu et al. 2016), other example are observations performed by Foster et al. (2014) in the infrared and of the $NH_3\,(1,1)$ and $NH_3\,(2,2)$. We found that, in general, these works are in good agreement with the results obtained using the GBT data of G34 for the ammonia transitions. Xu et al. (2016) find only one velocity component within a range of 53 - 63 $\mathrm{km\,s^{-1}}$ when analysing G34 using $C^{18}O$, while the data of NH_3 allows to resolve for three different components in that same range of velocity.

Foster et al. (2014) use the $NH_3\,(1,1)$ and $NH_3\,(2,2)$ transitions and consider all of the G34 IRDC as a single entity. They find linewidths of the order of $3\,\mathrm{km\,s^{-1}}$ which seems to correspond to the obtained results for G34, since the contribution in linewidth is of about the same order of magnitude for this region (see Table 3.2). Another interesting result from the same authors is with respect to the kinetic temperature, since traced with the ammonia it corresponds to a mean value of ~ 15 K, which differs lightly to the values found for each filamentary component which lie within the range of 18 – 21 K. This difference in both linewidths and temperature values with respect to the present work can be understood due to the fact that, unlike Foster et al. (2014), we have analyzed the IRDC separating each identified velocity component.

The stability of the filament is of rather importance for comparing the resulting super-critical instabilities found due to an observed $\alpha_v \lesssim 2$ for all the velocity components of the cloud. Foster et al. (2014) find the mass per unit length from the column density map and obtain that $\alpha_v < 1$ which suposses a state of unstable towards collapse. This is also calculated in Xu et al. (2016) but in a similar fashion that the one carried out in this work: by comparison of the M/L and $(M/L)_{crit}$ which results in the same outcome, the region its unstable, although one of the reasons it is not collapsing yet might be by the fact that turbulence might be helping to stabilize the filament.

In the case of G35 there is even more information to compare since it has been largely studied, for example we can mention the work of Henshaw et al. (2014) using IRAM PdBI observations of N_2H^+(1–0) and Jiménez-Serra et al. (2014) using $C^{13}O$ (1–0) and $C^{18}O$ (1–0). The kinematics studied in both works show that the IRDC G35 is composed of three different filaments with different central velocities (see Chapter 1), we can say that these subfilaments might correspond to at least the two filamentary velocity components found for G35 since their central velocity values are within the range shown for each subfilament mentioned in both works (43.7, 45.2 and 46.5 $\mathrm{km\,s^{-1}}$). Also, the two works, although using different tracers, find a global extended gradient of $\sim 0.8\,\mathrm{km\,s^{-1}\,pc^{-1}}$ which directly relates to the global velocity gradient of which is evident after seen the central velocity map for the main component 3 of G35 (see Figure 3.5).

In Henshaw et al. (2014), the authors define the main filament of G35 as filament 2, that they are later able to resolve and decompose into two substructures F2a and F2b along with a subfilament F3. Calculations of gradients for these components reveal magnitudes of $\sim 0.23\,\mathrm{km\,s^{-1}\,pc^{-1}}$ for F2a and $0.56\,\mathrm{km\,s^{-1}\,pc^{-1}}$ for F2b which directly coincide with the gradients of $\sim 0.18\,\mathrm{km\,s^{-1}\,pc^{-1}}$ for component 3 and $0.64\,\mathrm{km\,s^{-1}\,pc^{-1}}$ for component 1 respectively. Thus, it is affordable to say that subfilament F2a of Henshaw et al. (2014) is related with component 3 of our work, and that subfilament F2b is related with our component 1 which is embodied inside the main component. This might be confirmed by the fact that the mean centroid velocity of subfilaments F2a and F2b are about 45 and 46 $\mathrm{km\,s^{-1}}$ traced with N_2H^+, and this value fall within the range defined for our NH_3 main component which is 44.7 – 46.7 $\mathrm{km\,s^{-1}}$.

Also it is important to verify the nature of the gas motions in the region, so for a dense tracer such as N_2H^+(Jiménez-Serra et al. 2014; Henshaw et al. 2014) it is found that the gas motions are mildly supersonic, with a mean value $\sigma_{NT}/c_s = 1.5$ which is within the range of the values obtained for the filamentary velocity components of G35 (see Table 3.3).

The unstable characteristics of the filament is also confirmed in Henshaw et al. (2014) where the value of the mean virial parameter is of about 1.5, still being less than 2 which means a supercritical region.

In a general review, it is possible to comment that looking at the results of the NH_3 column densty maps, the peaks in column density for the different velocity components in both regions are related with the general location of both the protostellar and prestellar millimetric clumps identified by Rathborne, Jackson and Simon (2006), which are indicators of possible places where star formation is or is going to take place in the future.

4.2 Conclusions

A general study of the kinematics in two IRDCs noted as G34 and G35 was made using GBT data observations of the $NH_3\,(1,1)$ and $NH_3\,(2,2)$ transitions. Multiple velocity components were fitted into the spectra in order to find a set of line and physical parameters. A further analysis has been made to describe the stability of the regions and some other aspects such as rotational temperature measurement and density profile.

The general conclusions can be summarized as follows:

1. Both regions have multiple components, resulting from the fit of the ammonia spectra, some of which, are related with subfilamentary structures and other ones have a more compact form. These different components might be provided by the characteristic of IRDCs of being composed of subfilament structures. Three velocity components have been determined for G34 and four for G35.
2. Of these components it has been established which ones have filamentary shapes: components 1 and 2 for G34 and components 2 and 3 for G35.
3. The filamentary components of both G34 and G35 present NH_3 column density values within the range of $0.282 \times 10^{15} - 1.074 \times 10^{15}\,\mathrm{cm^{-2}}$ with the peaks in column density intimately related with millimeter prestellar and protostellar clumps identified in earlier works (e.g. Rathborne, Jackson and Simon 2006).

4. Derived rotational temperatures ($T_{\rm rot}$) were found for each of the IRDCs: for G34 the range is $T_{\rm rot}$ is 16 - 22 K, for G35 the range is 12 - 17 K which are typical IRDC temperatures.
5. Density profiles of these regions with respect to different column density peaks are in good agreement with the isothermal cylinder model with a power law index of 1.5. The fitted model gives central densities of 4.98×10^4 cm^{-3} for G34 and 1.96×10^4 cm^3 for G35.
6. For G34 local velocity gradients were found and for G35 an extended global gradient was obtained which matched the previous works carried out about this region. An oscillatory pattern, similar to the one found for filaments in Taurus (Hacar and Tafalla 2011), was spotted for G34 and G35 which might be related to core-forming motion along the axis of the filaments.
7. This near IRDCs both present gas motions that are mildly supersonic with most dense gas with $\sigma_{NT}/c_s > 1$. The highest values of σ_{NT}/c_s in the filamentary components of G34 and G35 appear to be related with the positions of the millimeter clumps.
8. Both G34 and G35 are massive objects, with the mass of the components being within the 50 - 5500 $M_\odot$ range. Calculations of the virial parameter α_v for the filamentary velocity component show that these are supercritical regions that might be stabilized by turbulence effects.
9. In general, this regions do not meet the characteristics of low-mass star forming regions due to the latter pc like scales and less massive environments. However they are considered fairly in agreement with typical parameter values of regions of high-mass star formation.

4.3 Future Work

A more complete statistical analysis concerning IRDCs is left for a future work, using NH_3 observations from the GBT towards three other filamentary structures: G24.96-00.15, SDC34.539+0.536 and Hi-GAL 47.10+0.28. Also, left for future work in the deeper analysis of the oscillatory paterns related to core-forming motions in the filaments.

Bibliography

André, P., A. Men'shchikov, S. Bontemps et al. 2010. "From filamentary clouds to prestellar cores to the stellar IMF: Initial highlights from the Herschel Gould Belt Survey." *A & A* 518:L102.

André, P., J. Di Francesco, D. Ward-Thompson et al. 2014. "From Filamentary Networks to Dense Cores in Molecular Clouds: Toward a New Paradigm for Star Formation." *PP VI* pp. 27–51.

Arzoumanian, D., P. André, P. Didelon et al. 2011. "Characterizing interstellar filaments with Herschel in IC 5146." *A & A* 529:L6.

Benedettini, M., E. Schisano, S. Pezzuto et al. 2015. "Filaments in the Lupus molecular clouds." *MNRAS* 453:2036–2049.

Bertoldi, F. and C. F. McKee. 1992. "Pressure-confined clumps in magnetized molecular clouds." *APJ* 395:140–157.

Busquet, G., Q. Zhang, A. Palau et al. 2013. "Unveiling a Network of Parallel Filaments in the Infrared Dark Cloud G14.225-0.506." *APJL* 764:L26.

Butler, M. J. and J. C. Tan. 2009. "Mid-Infrared Extinction Mapping of Infrared Dark Clouds: Probing the Initial Conditions for Massive Stars and Star Clusters." *APJ* 696:484–497.

Carey, S. J., F. O. Clark, M. P. Egan et al. 1998. "The Physical Properties of the Midcourse Space Experiment Galactic Infrared-dark Clouds." *APJ* 508:721–728.

Egan, M. P., R. F. Shipman, S. D. Price et al. 1998. "A Population of Cold Cores in the Galactic Plane." *APJ* 494:L199–L202.

Estalella, R. 2017. "HfS, Hyperfine Structure Fitting Tool." *PASP* 129(2):025003.

Estalella, R. and G. Anglada. 1996. *Introducción a la Física del Medio Interestelar*. 1 ed. Edicions de la Universitat de Barcelona.

Foster, J. B., H. G. Arce, M. Kassis et al. 2014. "Distributed Low-mass Star Formation in the IRDC G34.43+00.24." *APJ* 791:108.

Foster, Jonathan B., Erik W. Rosolowsky, Jens Kauffmann et al. 2009. "Dense Cores in Perseus: The Influence of Stellar Content and Cluster Environment." *APJ* 696(1):298.

Goldsmith, P. F., M. Heyer, G. Narayanan et al. 2008. "Large-Scale Structure of the Molecular Gas in Taurus Revealed by High Linear Dynamic Range Spectral Line Mapping." *APJ* 680:428–445.

Gómez, G. C. and E. Vázquez-Semadeni. 2014. "Filaments in Simulations of Molecular Cloud Formation." *APJ* 791:124.

Hacar, A., J. Alves, M. Tafalla et al. 2017. "Gravitational collapse of the OMC-1 region." *A & A* 602:L2.

Hacar, A., J. Kainulainen, M. Tafalla et al. 2016. "The Musca cloud: A 6 pc-long velocity-coherent, sonic filament." *A & A* 587:A97.

Hacar, A. and M. Tafalla. 2011. "Dense core formation by fragmentation of velocity-coherent filaments in L1517." *A & A* 533:A34.

Hacar, A., M. Tafalla, J. Kauffmann et al. 2013. Cores, Filaments, and Bundles: Hierarchical core formation in the B213 filament in Taurus. In *Protostars and Planets VI Posters*.

Hatchell, J., J. S. Richer, G. A. Fuller et al. 2005. "Star formation in Perseus. Clusters, filaments and the conditions for star formation." *A & A* 440:151–161.

Henshaw, J. D., P. Caselli, F. Fontani et al. 2013. "Complex, quiescent kinematics in a highly filamentary infrared dark cloud." *MNRAS* 428:3425–3442.

Henshaw, J. D., P. Caselli, F. Fontani et al. 2014. "The dynamical properties of dense filaments in the infrared dark cloud G035.39-00.33." *MNRAS* 440:2860–2881.

Ho, P. T. P. and C. H. Townes. 1983. "Interstellar ammonia." *ARAA* 21:239–270.

Jackson, J. M., S. C. Finn, E. T. Chambers et al. 2010. "The "Nessie" Nebula: Cluster Formation in a Filamentary Infrared Dark Cloud." *APJL* 719:L185–L189.

Jiménez-Serra, I., P. Caselli, F. Fontani et al. 2014. "Gas kinematics and excitation in the filamentary IRDC G035.39-00.33." *MNRAS* 439:1996–2013.

Jiménez-Serra, I., P. Caselli, J. C. Tan et al. 2010. "Parsec-scale SiO emission in an infrared dark cloud." *MNRAS* 406:187–196.

Kauffmann, J., T. Pillai and P. F. Goldsmith. 2013. "Low Virial Parameters in Molecular Clouds: Implications for High-mass Star Formation and Magnetic Fields." *APJ* 779:185.

Kurayama, T., A. Nakagawa, S. Sawada-Satoh et al. 2011. "Annual Parallax Measurements of an Infrared Dark Cloud, MSXDC G034.43+00.24 with VERA." *PASJ* 63:513–525.

Molinari, S., B. Swinyard, J. Bally et al. 2010. "Clouds, filaments, and protostars: The Herschel Hi-GAL Milky Way." *A & A* 518:L100.

Myers, P. C. 2009. "Filamentary Structure of Star-forming Complexes." *APJ* 700:1609–1625.

Nakamura, F., T. Miura, Y. Kitamura et al. 2012. "Evidence for Cloud-Cloud Collision and Parsec-scale Stellar Feedback within the L1641-N Region." *APJ* 746:25.

Nguyen Luong, Q., F. Motte, M. Hennemann et al. 2011. "The Herschel view of massive star formation in G035.39-00.33: dense and cold filament of W48 undergoing a mini-starburst." *A & A* 535:A76.

Ostriker, J. 1964. "The Equilibrium of Polytropic and Isothermal Cylinders." *APJ* 140:1056.

Padoan, P., A. Goodman, B. T. Draine et al. 2001. "Theoretical Models of Polarized Dust Emission from Protostellar Cores." *APJ* 559:1005–1018.

Perault, M., A. Omont, G. Simon et al. 1996. "First ISOCAM images of the Milky Way." *A & A* 315:L165–L168.

Pillai, T., F. Wyrowski, S. J. Carey et al. 2006. "Ammonia in infrared dark clouds." *A & A* 450:569–583.

Ragan, S. E., E. A. Bergin and R. A. Gutermuth. 2009. "Detection of Structure in Infrared-Dark Clouds with Spitzer: Characterizing Star Formation in the Molecular Ring." *APJ* 698:324–349.

Rathborne, Jill M., J. M. Jackson, E. T. Chambers et al. 2005. "Massive protostars in the infrared dark cloud msxdc g034.43+00.24." *APJ* 630:L181–L184.

Rathborne, Jill M., J. M. Jackson and R. Simon. 2006. "Infrared dark clouds: precursors to star clusters." *APJ* 641:389–405.

Schneider, N., T. Csengeri, S. Bontemps et al. 2010. "Dynamic star formation in the massive DR21 filament." *A & A* 520:A49.

Schneider, S. and B. G. Elmegreen. 1979. "A catalog of dark globular filaments." *APJS* 41:87–95.

Sepúlveda, I. 1993. Estudio en NH_3 de Regiones de Formación Estelar. Undergraduate honors thesis Universitat de Barcelona Facultat de FÃsica: . Department d'Astronomia i Meteorologia.

Simon, R., J. M. Jackson, J. M. Rathborne et al. 2006. "A Catalog of Midcourse Space Experiment Infrared Dark Cloud Candidates." *APJ* 639:227–236.

Simon, R., J. M. Rathborne, R. Y. Shah et al. 2006. "The Characterization and Galactic Distribution of Infrared Dark Clouds." *APJ* 653:1325–1335.

Sokolov, V., K. Wang, J. E. Pineda et al. 2017. "Temperature structure and kinematics of the IRDC G035.39-00.33." *ArXiv e-prints* .

Stodólkiewicz, J. S. 1963. "On the Gravitational Instability of Some Magneto-Hydrodynamical Systems of Astrophysical Interest. Part III." *ACTAA* 13:30–54.

Ungerechts, H., G. Winnewisser and M. Gaida. 1985. Star counts and ammonia observations in the central Taurus region. In *Lecture Notes in Physics, Berlin Springer Verlag*, ed. G. Serra. Vol. 237 of *Lecture Notes in Physics, Berlin Springer Verlag* pp. 78–80.

Xu, J.-L., D. Li, C.-P. Zhang et al. 2016. "Gas Kinematics and Star Formation in the Filamentary IRDC G34.43+0.24." *APJ* 819:117.